










Feedback and ionized gas outflows in four low-radio power AGN at $z \sim 0.15$

L. Ulivi^{1,2,3} , G. Venturi^{5,4,3} , G. Cresci^{2,3} , A. Marconi^{2,3}, C. Marconcini^{2,3}, A. Amiri⁶ , F. Belfiore³ , E. Bertola³ , S. Carniani⁵, Q. D'Amato³, E. Di Teodoro^{2,3}, M. Ginolfi^{3,7} , A. Girdhar^{7,8,9}, C. Harrison⁹, R. Maiolino^{10,11,12}, F. Mannucci³, M. Mingozzi¹³, M. Perna¹⁴ , M. Scialpi^{1,2,3}, N. Tomicic^{2,3}, G. Tozzi^{2,3} , and E. Treister⁴

¹ University of Trento, Via Sommarive 14, 38123 Trento, Italy
e-mail: lorenzo.ulivi@unitn.it

² Università di Firenze, Dipartimento di Fisica e Astronomia, Via G. Sansone 1, 50019 Sesto F.no, Firenze, Italy

³ INAF – Osservatorio Astrofisico di Arcetri, Largo E. Fermi 5, 50125 Firenze, Italy

⁴ Instituto de Astrofísica, Facultad de Física, Pontificia Universidad Católica de Chile, Casilla 306, Santiago 22, Chile

⁵ Scuola Normale Superiore, Piazza dei Cavalieri 7, 56126 Pisa, Italy

⁶ Department of Physics, University of Arkansas, 226 Physics Building, 825 West Dickson Street, Fayetteville, AR 72701, USA

⁷ European Southern Observatory, Karl-Schwarzschild-Str. 2, 85748 Garching, Germany

⁸ Ludwig Maximilian Universität, Professor-Huber-Platz 2, 80539 Munich, Germany

⁹ School of Mathematics, Statistics and Physics, Newcastle University, Newcastle upon Tyne NE1 7RU, UK

¹⁰ Kavli Institute for Cosmology, University of Cambridge, Madingley Road, Cambridge CB3 0HA, UK

¹¹ Cavendish Laboratory, Astrophysics Group, University of Cambridge, 9 JJ Thomson Avenue, Cambridge CB3 0HE, UK

¹² Department of Physics & Astronomy, University College London, Gower Street, London WC1E 6BT, UK

¹³ Space Telescope Science Institute, 3700 San Martin Drive, Baltimore, MD 21218, USA

¹⁴ Centro de Astrobiología, (CAB, CSIC-INTA), Departamento de Astrofísica, Cra. de Ajalvir Km. 4, 28850 Torrejón de Ardoz, Madrid, Spain

Received 11 July 2023 / Accepted 18 January 2024

ABSTRACT

An increasing number of observations and simulations suggests that low-power ($<10^{44}$ erg s^{-1}) jets may be a significant channel of feedback produced by active galactic nuclei (AGN), but little is known about their actual effect on their host galaxies from the observational point of view. We targeted four luminous type 2 AGN hosting moderately powerful radio emission ($\sim 10^{44}$ erg s^{-1}), two of which and possibly a third are associated with jets, with optical integral field spectroscopy observations from the Multi Unit Spectroscopic Explorer (MUSE) at the Very Large Telescope (VLT) to analyze the properties of their ionized gas as well as the properties and effects of ionized outflows. We combined these observations with Very Large Array (VLA) and e-MERLIN data to investigate the relations and interactions between the radio jets and host galaxies. We detected ionized outflows as traced by the fast bulk motion of the gas. The outflows extended over kiloparsec scales in the direction of the jet, when present. In the two sources with resolved radio jets, we detected a strong enhancement in the emission-line velocity dispersion (up to 1000 km s^{-1}) perpendicular to the direction of the radio jets. We also found a correlation between the mass and the energetics of this high-velocity dispersion gas and the radio power, which supports the idea that the radio emission may cause the enhanced turbulence. This phenomenon, which is now being observed in an increasing number of objects, might represent an important channel for AGN feedback on galaxies

Key words. ISM: jets and outflows – galaxies: active – galaxies: jets – galaxies: kinematics and dynamics

1. Introduction

Active galactic nuclei (AGN) are thought to play a significant role in shaping the formation and evolution of galaxies, particularly at the high-mass end, through a series of processes known as AGN feedback (Silk & Rees 1998; Fabian 2012). This mechanism is considered an essential element in semianalytic models and hydrodynamic simulations of galaxy evolution because it helps explain a number of the observed properties of galaxies that can otherwise not be accounted for (e.g., Kormendy & Richstone 1995; Häring & Rix 2004; Marconi et al. 2004; Ferrarese & Merritt 2000; Gebhardt et al. 2000; Fabian 2012).

AGN feedback is thought to operate in two main modes. In the radiative mode, also known as quasar or wind mode,

in which the radiation emitted by the accreting central supermassive black hole (SMBH) drives powerful outflows that can suppress star formation in the host galaxy by removing, displacing, or heating the interstellar medium (ISM; e.g., Ciccone et al. 2014; Harrison et al. 2014; Cresci et al. 2015; Carniani et al. 2015; Dall’Agnol de Oliveira et al. 2021). The second mode is the kinetic mode, also known as radio mode, in which AGN feedback occurs through powerful ($\geq 10^{45}$ erg s^{-1}) extended (~ 100 kpc) jets launched directly from the central AGN (Fabian 2012). These radio jets are thought to be crucial for AGN feedback because they are able to heat the circumgalactic medium (CGM) and prevent the cooling of gas, thereby suppressing the formation of new stars (e.g., McNamara & Nulsen 2012). They are also capable of launching energetic outflows that can remove gas from the host galaxy (e.g., Nesvadba et al. 2008;

Vayner et al. 2017). Recent studies have found from both observational (Combes et al. 2013; García-Burillo et al. 2014; Cresci et al. 2015; Jarvis et al. 2019, 2021; Molyneux et al. 2019; Venturi et al. 2021, 2023; Girdhar et al. 2022; Audibert et al. 2023; Peralta de Arriba et al. 2023) and theoretical (Mukherjee et al. 2016, 2018a,b; Mandal et al. 2021; Meenakshi et al. 2022) perspectives that low-power ($<10^{44}$ erg s $^{-1}$) and compact jets (lower than 1 kpc) can also have a significant impact on their host galaxy by injecting turbulence in the ISM and accelerating outflows.

From an observational standpoint, classical models of feedback are not always able to fully explain the observational properties of galaxies. This means that it is important to identify and understand new mechanisms of feedback. In a recent study, Venturi et al. (2021) identified a potentially significant mechanism of AGN feedback on the galaxy ISM associated with the presence of low-power ($<10^{44}$ erg s $^{-1}$) compact (~ 1 kpc) radio jets. Local Seyfert galaxies hosting low-power jets oriented at a low inclination relative to the disk of the galaxy have been found to exhibit an increase in the line width of the main emission lines perpendicular to the radio jet, without obvious signs of a strong systematic velocity shift of the line centroid. This enhanced velocity dispersion may be caused by the high levels of turbulence that are injected into the ISM by the jet. Although this phenomenon was previously observed in other local Seyfert galaxies (e.g., Finlez et al. 2018; Couto et al. 2014; Shimizu et al. 2019; Freitas et al. 2018; Riffel et al. 2015; Bianchin et al. 2021; Ruschel-Dutra et al. 2021), the possible connection to the jet was thoroughly investigated, and other explanations were proposed, such as beam smearing, equatorial outflows from the accretion disk, or multidirectional outflows. In some cases, the enhanced perpendicular line width was observed not only in ionized gas, but also in molecular gas, although the enhancement is not as strong as in the ionized phase (e.g., Riffel et al. 2015; Shimizu et al. 2019; Bianchin et al. 2021; Girdhar et al. 2022; Audibert et al. 2023). The hypothesis that jet-driven shocks might cause the increase in the velocity dispersion is further supported by recent simulations, which revealed that the interaction between jets and the ISM depends on the properties of the jet, such as inclination and power (Mukherjee et al. 2018a). Previous works (Mullaney et al. 2013; Molyneux et al. 2019; Woo et al. 2016) have shown that AGN with moderate radio luminosity ($L_{1.4\text{GHz}} = 10^{23-25}$ W Hz $^{-1}$) can significantly affect the [OIII] profile, leading to an enhancement of the line width.

The main goal of this paper is to examine the impact of moderately luminous jets on the host galaxy and to explore the interplay between the AGN and its surroundings. First, we investigate the properties of ionized galactic outflows and the physical conditions of the ionized gas in four type 2 AGN at $z \sim 0.15$ in detail using spatially resolved optical integral field spectroscopic (IFS) observations from the Multi Unit Spectroscopic Explorer (MUSE) at the Very Large Telescope (VLT). We then compare our MUSE observations with radio-emission maps from the Very Large Array (VLA) and e-MERLIN to investigate the effects of moderate-power radio jets ($\sim 10^{44}$ erg s $^{-1}$) on the host galaxy, extending the work of Venturi et al. (2021) on low-power radio (i.e., $\lesssim 10^{44}$ erg s $^{-1}$) AGN jets to higher jet luminosities.

This paper is structured as follows. We present the sample selection, the data reduction, and the spectroscopic analysis in Sects. 2 and 3, respectively. In Sect. 4 we present the results of our analysis, including emission-line flux and kinematic maps, gas-excitation diagrams, and a characterization of the outflowing gas

through computing their energetics. We then examine the effects of radio jets on the host galaxy in detail and compute the mass and energy of the gas involved in the jet-ISM interaction. We compare our results to those of Venturi et al. (2021) as well as to other results from the literature in Sect. 5. Finally, we summarize our conclusions in Sect. 6.

2. Sample selection and data reduction

We analyzed MUSE data of four type 2 AGN (J1000+1242, J1010+1413, J1010+0612, J1100+0846; see Table 1). These AGN were selected from Jarvis et al. (2019) for their high bolometric luminosity ($>10^{45}$ erg s $^{-1}$; placing these sources in the quasar regime), the extended ionized outflows in [OIII]5007 and the radio emission, with the aim to study the properties of the outflows and the relation between the ionized gas and radio jets, when resolved. The AGN in our sample are classified as radio quiet according to the criterion established by Xu et al. (1999), which is based on the correlation between the radio luminosity at 5 GHz and the [OIII]5007 luminosity. Despite this classification, they exhibit moderate radio luminosity ($\sim 10^{24}$ W Hz $^{-1}$ at 1.4 GHz) and host jets in most cases. To study the morphology of the radio emission and its detailed structures, we used the VLA and e-MERLIN interferometric radio observations presented in Jarvis et al. (2019). In two out of four galaxies (J1000+1242 and J1010+1413), the radio emission that is associated with jets (Jarvis et al. 2019) is extended on 10–20 kpc scales. This allowed us to study the relation between the radio jet and the ionized gas in detail. For J1100+0846, only an ambiguous extended feature (~ 0.8 kpc north of the nucleus) is detected with e-MERLIN, while for J1010+0612, the radio emission is not resolved ($\lesssim 0.3$ kpc). Consistently with Jarvis et al. (2019), we computed the noise using 8σ clipping repeated ten times in a region 50 times the size of the beam ($1''$ for VLA and $0.25''$ for e-MERLIN.) For J1000+1242, J1010+1413, and J1100+0846, we also exploited *Hubble* Space Telescope (HST) WFC3 and ACS images obtained with the F621M, F689M, and FR551N filters. These filters have a spectral coverage of ~ 800 , 800 , and 200 \AA around the central wavelengths 6218, 6876, and 5510 \AA , respectively (Rodrigo et al. 2012). For the redshifts of our targets, these filters trace the continuum emission of the galaxies. The HST images were retrieved from the *Hubble* Legacy Archive. The radio maps and HST images are shown in Fig. 1.

The MUSE data of the four galaxies presented in this work belong to ESO program 0104.B-0476 (PI G. Venturi). All the observations were acquired in seeing-limited wide-field mode (WFM), which covers a field of view (FOV) of $1' \times 1'$ with a sampling of 0.2 arcsec/spaxel. The data consist of two observing blocks (OBs) for J1010+1413 and J1010+0612 for a total of eight exposures of 700 s each, one OB for J1100+0846 for a total of six exposures of 450 s each, and five OBs for J1000+1242 for a total of 16 exposure of 700 s each; 5 of these 16 exposures were discarded during the data reduction due to the significantly worse seeing ($>1''$), and we thus combined only 11 exposures to produce the data cube employed in this work for J1000+1242. We estimated the atmospheric optical seeing at the zenith at 500 nm (DIMM) by averaging the mean of DIMM seeing at the start and end of the observation over all the exposures. The main technical details of the observations are reported in Table 1. Subsequent exposures were dithered and rotated by 90 degrees in order to remove the artifacts produced by the 24 channels associated with each IFU, as well as to optimize cosmic-ray removal and background

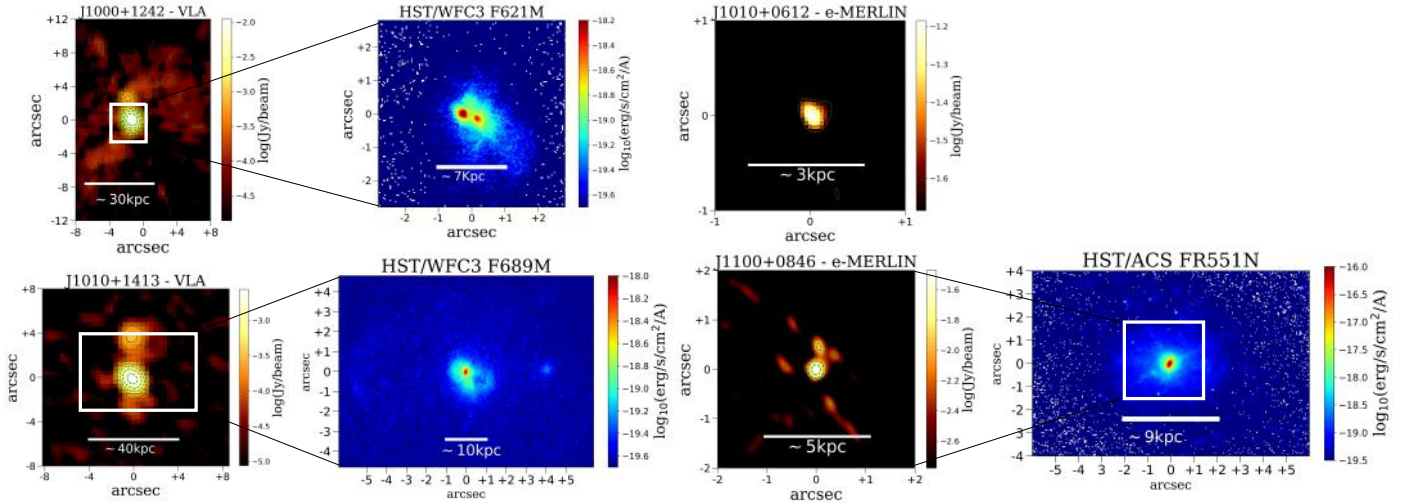


Fig. 1. Left panels: low-resolution (~ 1 arcsec HPBW) 6 GHz VLA radio images from [Jarvis et al. \(2019\)](#) for J1000+1242 (top) and J1010+1413 (bottom). Right panels: e-MERLIN data (~ 0.2 arcsec HPBW) for J1010+0612 (top) and J1100+0846 (bottom). All panels show a zoomed-in inset with the optical images from HST/WFC3. The J1010+0612 radio data are not resolved, and no HST data are available for this AGN. The green contours represent $[2, 4, 8, 16, 32, 64, 128]\sigma$ for the VLA images and $[8, 16, 32, 64, 128]\sigma$ for e-MERLIN.

Table 1. Basic properties of the four AGN in our sample.

Name	RA ⁽¹⁾ [hh:mm:ss]	Dec ⁽²⁾ [dd:mm:ss]	z ⁽³⁾	D_L ⁽⁴⁾ [Mpc]	Date ⁽⁵⁾ [DD-MM-YYYY]	DIMM ⁽⁶⁾ [arcsec]	N frames ⁽⁷⁾	t_{exp} ⁽⁸⁾ [s]	t_{tot} ⁽⁹⁾ [s]
J1000+1242	10:00:13.14	+12:42:26.2	0.1480	732	18-02-2020	0.73	11	700	7700
J1010+1413	10:10:22.95	+14:13:00.9	0.1992	1010	29-01-2020	0.62	8	700	5600
J1010+0612	10:10:43.36	+06:12:01.4	0.0984	468	02-04-2020	0.78	8	700	5600
J1100+0846	11:00:12.38	+08:46:16.3	0.1005	483	03-03-2020	1.03	6	450	2700

Notes. ⁽¹⁾Right Ascension. ⁽²⁾Declination. ⁽³⁾Estimated redshift from [Harrison et al. \(2014\)](#). ⁽⁴⁾Luminosity distance in Mpc taken from NASA/IPAC Extragalactic Database (<https://ned.ipac.caltech.edu/>). ⁽⁵⁾Starting date of the observations. ⁽⁶⁾Mean DIMM seeing measured during the observations at 500 nm and at zenith. ⁽⁷⁾Number of exposures. ⁽⁸⁾Exposure time per exposure. ⁽⁹⁾Total exposure time on target.

subtraction. The sky emission was subtracted using a sky spectrum extracted from regions free of target emission in the science frame.

The data reduction and exposure combination were carried out with the ESO MUSE pipeline version v1.6 using ESO Reflex, which provides a graphical and automated way to execute the reduction recipes with ESORex (for details, see [Weilbacher et al. 2020](#)).

3. Spectroscopic analysis

In this section, we briefly describe the key steps of the analysis of the MUSE optical IFS data cubes to study the emission lines arising from the ISM. The details of the spectral analysis performed in this study can be found in previous works (e.g., [Marasco et al. 2020](#); [Tozzi et al. 2021](#); [Cresci et al. 2023](#)). Before the emission lines were fit, some pre-processing steps were required. First, it was necessary to remove the contribution of the spatially unresolved AGN and the stellar continuum. To do this, we performed a Voronoi tessellation ([Cappellari & Copin 2003](#)) to obtain spatial bins with a signal-to-noise ratio (hereafter, S/N) > 5 in each wavelength channel (1.25 \AA wide). To remove the continuum, we considered a model that included the continuum emission from the stars and AGN and the line emission modeled with a combination of Gaussian functions. Because our objects are type 2 AGN, we did not include the

unresolved emission of the broad line region (BLR) from the core of the AGN in the model. We used the MILES stellar population synthesis templates to model the stellar continuum ([Sánchez-Blázquez et al. 2006](#); [Falcón-Barroso et al. 2011](#)). We also adopted a third-order multiplicative polynomial and an additive polynomial of degree between 5 and 7, depending on each target, to reproduce the low contribution of the AGN continuum and the spectral shape, which might be distorted by the reddening. We fit the model to the observed spectra employing the penalized pixel-fitting code (PPX; [Cappellari & Emsellem 2004](#)). After constructing the total model, we finally subtracted the continuum from the cube spaxel by spaxel and we rescaled the modeled continuum emission obtained in each Voronoi bin to the median of the observed continuum in each spaxel. In this way, we obtained a cube that only contained the contribution of the ionized gas emission lines. We smoothed each slice of the cube with a Gaussian with a dispersion $\sigma_{\text{smooth}} = 1$ spaxel, corresponding to 0.2 arcsec. This allowed us to better investigate the ionized gas by enhancing the S/N while minimizing the degradation of spatial resolution. Then we modeled the emission lines in each spaxel, including $H\alpha$, $H\beta$, the oxygen doublets $[\text{OIII}]\lambda 4959, 5007$ and $[\text{OI}]\lambda 6300, 6364$, $[\text{NII}]\lambda 6548, 6584$, and $[\text{SII}]\lambda 6717, 6731$. We parameterized each line with up to three Gaussian components. To reduce the parameter degeneracies, we kept the velocity and the velocity dispersion of each Gaussian component fixed for all lines, while the flux parameters were left

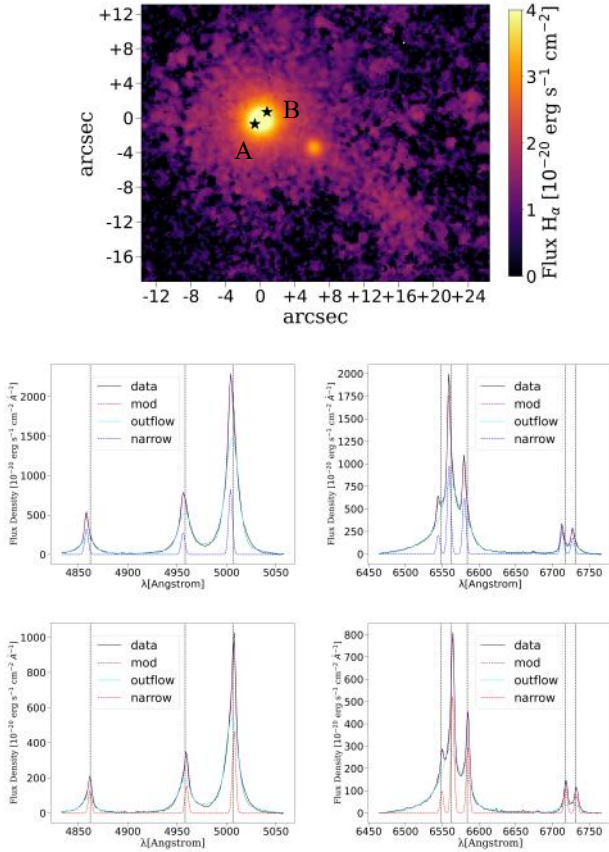


Fig. 2. Upper panel: flux density map of J1010+0612 from MUSE. Bottom panels: spectra extracted from regions A and B marked with the black stars in the upper panel. The first column shows the spectral range that includes H β and [OIII] doublet, and the second column displays the range that includes the H α , [NII], and [SII] doublets. The black lines represent the data subtracted from the continuum emission, as described in Sect. 2, the purple lines show the total model, the cyan lines show the broad components, and the red (up) and blue (bottom) lines show the narrow components obtained by decoupling the line profiles, as described in Sect. 3.

free to vary, with the exception of the [OIII] and [NII] doublets, whose flux ratio was kept fixed to the values imposed by atomic physics (0.343 and 0.338, respectively¹). We performed three different fittings by using one, two, and three Gaussian components per emission line. A Kolmogorov-Smirnov (K-S) test on the residuals of the fit was carried out to define the minimum number of components required to provide an acceptable fit in each spaxel (Marasco et al. 2020). As a final step, we attempted to decouple the kinematics of the ISM by separating the different contributions to the emission line profile (e.g., the rotation or debris merging from the outflows and the gas with high turbulence) in order to assign a physical meaning to each component and study each of them separately. There is no unique criterion for labeling a single component due to the different nature of the components, but we classified them into narrow or broad components depending on the velocity dispersion of each Gaussian component. Note that ‘broad’ should not be confused with the broad emission lines typical of type 1 AGN, which are emitted from the BLR. For the sources for which a rotating disk is clearly observed (J1010+0612 and J1100+0846), we set the

threshold value for the velocity dispersion above which we classified the components as broad and below which we classified them as narrow, to be 50 km s⁻¹ higher than the maximum value found for the stellar velocity dispersion (150–200 km s⁻¹) to take into account that the ionized gas in the disk could be more turbulent than the stellar kinematics. We stress that when fitting three Gaussian components to the emission lines, this approach could result in defining either one component as narrow and two as broad or two as narrow and one as broad. Figure 2 shows a clear example of the spectral decoupling of the emission line profiles between narrow and broad components in J1010+0612. The narrow component represents the emission from the disk while the blueshifted broad component represents the approaching outflow. For J1010+1413 and J1000+1242 we set the thresholds to different values to decouple the line profile, 350 and 250 km s⁻¹, respectively, because the stellar kinematics does not show clear rotational features and the ISM kinematics appears to be more complex.

4. Results

In this section, we present the flux, kinematic, and emission-line ratio maps of the ionized gas for the four targets in our sample. We mainly focus on the brightest emission line [OIII] λ 5007. We present both [OIII] and H α maps when they show very different characteristics, as in J1100+0846 and J1010+0612. We also present for each target the flux of the broad component of H α that we used to determine the properties of outflowing gas. Moreover, we also provide the moment 0, moment 1, and moment 2 maps, which were calculated on the whole modeled line profile (consisting of either one, two, or three Gaussians). The flux maps were not corrected for the extinction.

4.1. J1000+1242

J1000+1242 is an obscured quasar at $z \sim 0.148$ ($1'' \sim 3.5$ kpc). The ionized gas morphology shows unambiguous evidence of a merger event, as indicated by the elongated tidal tails (Fig. 3). In addition, data from HST/WC3 *F621M* (Fig. 1) reveal two distinct nuclear emission sources separated by approximately 1.5 kpc (Jarvis et al. 2019). These sources could either represent the double AGN resulting from the merger or the two opposite sides of the NLR obscured by a dusty circumnuclear ring. However, they are not spatially resolved in our MUSE data. An [OIII] bright region tracing the ionized gas is located in correspondence to the radio structures, as found in Jarvis et al. (2019), suggesting a possible connection between the ionized gas and the radio-emitting regions (as in, e.g., Riffel et al. 2014; Rodríguez-Ardila et al. 2017; May & Steiner 2017; May et al. 2018, 2020; Cresci et al. 2023; Venturi et al. 2021). The moment 0 map also reveals a tidal tail extending for about 20 arcsec in the southern region. It is predominantly observed in the [OIII] line and might be due to the superposition of two distinct tails. These tails also display distinct kinematic properties. Specifically, the easternmost tail exhibits a velocity of 200 km s⁻¹, but in contrast, the westernmost fainter tail shows a velocity from approximately 100–150 km s⁻¹ in its southern end that gradually decreases towards 0 km s⁻¹ as it extends northward (Fig. 3). The velocity field of the ionized gas also reveals two distinct blueshifted regions with velocities of ~ -200 km s⁻¹ located NE and SE of the nucleus, and a redshifted region located NW of it. This velocity field might be due to the twisting of the elongated tidal tails.

¹ We retrieved the ratios from <https://www.nist.gov/pml/atomic-spectra-database> (Kramida et al. 2023).

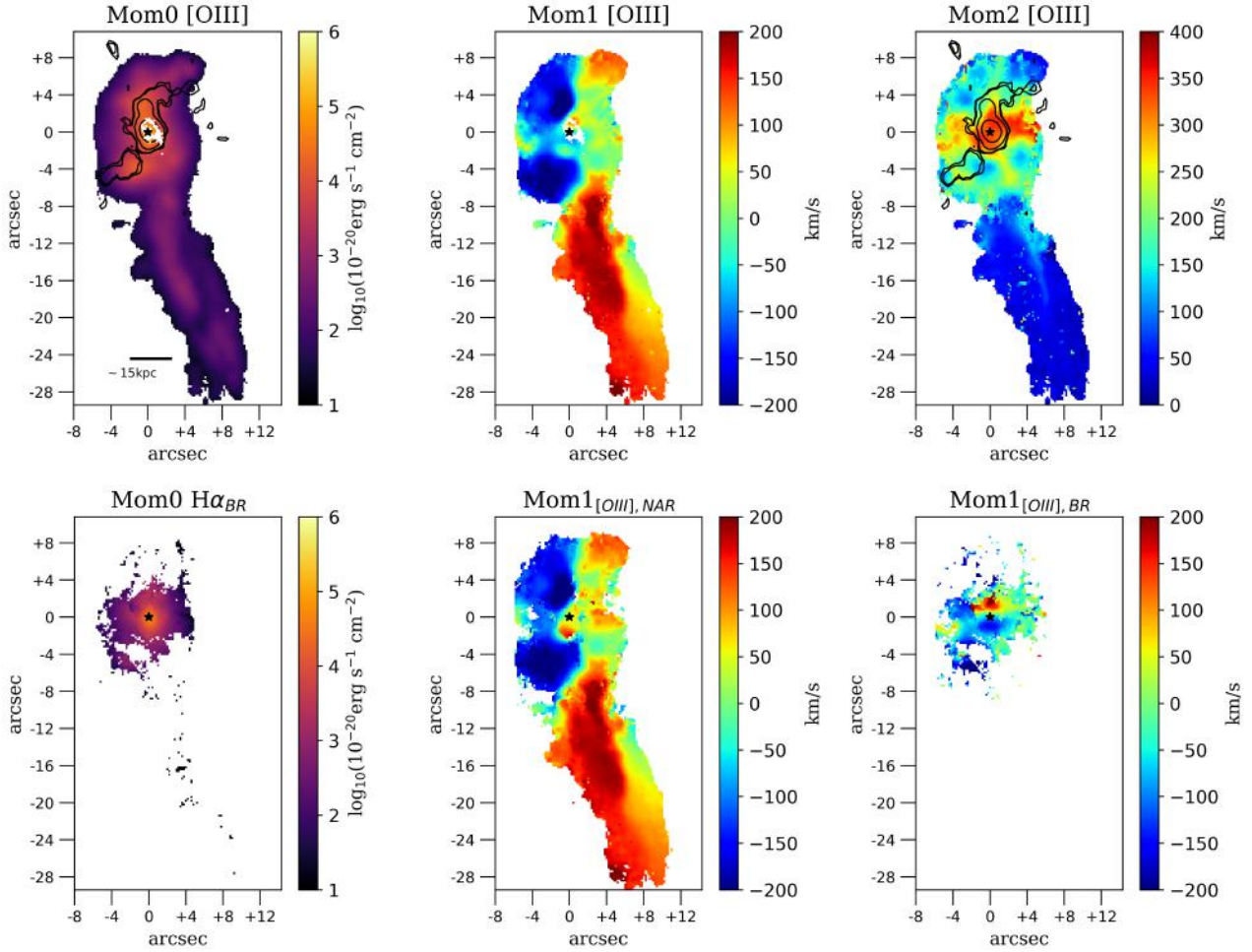


Fig. 3. Kinematics of the [OIII] line emission in J1000+1242. The upper panels show the flux (moment 0), velocity (moment 1), and velocity dispersion (moment 2) of the whole line profile. The lower panels show the flux of the broad component of H α , the velocity of the [OIII] narrow component (middle), and the velocity of the [OIII] broad component (right) obtained by decoupling the line profile. The black stars indicate the centers of the AGN. The black contours of VLA 6 GHz low resolution ($\sim 1''$ beam) vary from 0.07 to 2 mJy beam $^{-1}$. The white contours represent the HST continuum. An S/N cut of 3 has been applied to the maps for each line.

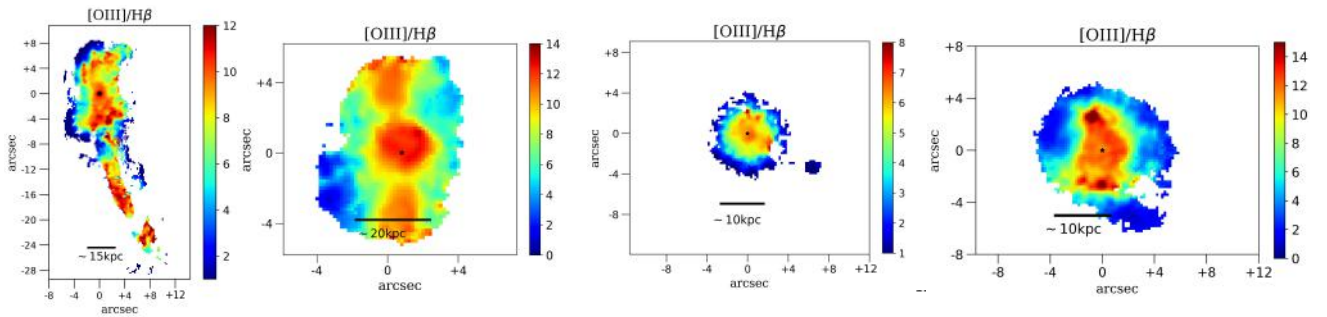


Fig. 4. [OIII]/H β . From left to right: J1000+1242, J1010+1413, J1010+0612, and J1100+0846. An S/N cut of 3 on the flux of each line has been applied to the maps.

The moment 2 map reveals an increase in the [OIII] velocity dispersion in the region near the nucleus, characterized by an elongated shape oriented W-E and perpendicular to the radio jet (see the radio contours in Fig. 3), similar to what was observed by Venturi et al. (2021) and references therein (see Sect. 5).

We computed the moment 1 of each spectrally decoupled component (narrow and broad; see Sect. 3), which are displayed in the bottom panels of Fig. 3. The [OIII] broad component shows a velocity gradient of ~ 350 km s $^{-1}$ that extends north-

south for 8–10 kpc. It is oriented like the radio jet and consistent with the slight [OIII] line asymmetry seen in Jarvis et al. (2019). We interpret the presence of the gradient of the [OIII] broad component, whose direction is consistent with the radio jet, as an outflow launched by the nuclear radio emission, which might demonstrating a direct connection between the radio jet and the outflows.

We also present a map of the [OIII]-to-H β flux ratio (Fig. 4), which is sensitive to the ionization state of the emitting gas. The

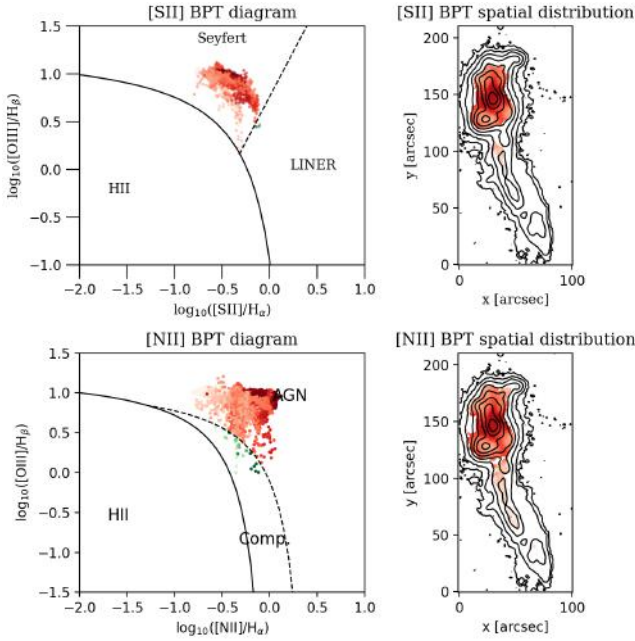


Fig. 5. Resolved S-BPT ($[\text{OIII}]/\text{H}\beta$ vs. $[\text{SII}]\lambda 6716,6731/\text{H}\alpha$) (top) and N-BPT ($[\text{OIII}]/\text{H}\beta$ vs. $[\text{NII}]\lambda 6584/\text{H}\alpha$) diagrams (bottom) of J1000+1242 for each spaxel with $S/N > 3$ in each line. The solid curves define the theoretical upper bound for the HII regions (Kewley et al. 2001). The dashed line in S-BPT represents the Kewley et al. (2006) demarcation between Seyfert galaxies and shocks or LINERs. The dashed curve in N-BPT represents the empirical classification by Kauffmann et al. (2003) to divide pure star-forming from Seyfert–H II composite objects. The black contours represent the moment 0 of $\text{H}\alpha$. The data points on the BPT diagram are colored differently to distinguish different regions. The intensity of the color is proportional to the moment 2 of $[\text{OIII}]$.

map reveals an extended structure, larger than 20 kpc, with high $[\text{OIII}]/\text{H}\beta$ (larger than 10), oriented in the same direction as the radio jets, indicating the presence of an AGN ionization cone. The value of $[\text{OIII}]/\text{H}\beta$ remains high at large distances from the nuclear sources. We do not exclude that shocks due to the jet that are cospatial with the ionization cone may also contribute to the ionization of the gas. To verify this, we used the $[\text{OIII}]/\text{H}\beta$ versus $[\text{SII}]/\text{H}\alpha$ and $[\text{OIII}]/\text{H}\beta$ vs. $[\text{NII}]/\text{H}\alpha$ BPT diagrams (e.g., Baldwin et al. 1981; Veilleux & Osterbrock 1987; Kewley et al. 2006; Lamareille 2010; Law et al. 2021; see Fig. 5). The map to the right, color-coded according to the location of each spaxel in the diagram to the left, indicates that the main ionization source are the AGN photons. The intensity of the color is proportional to the moment 2 of the $[\text{OIII}]$ line. We find that the ionization cone exhibits higher values of $[\text{OIII}]/\text{H}\beta$ and lower values of $[\text{SII}]/\text{H}\alpha$. Conversely, the tidal tails to the south, farther from the nucleus of the AGN, exhibit lower levels of ionization. In the $[\text{NII}]$ BPT diagram, the region with a higher velocity dispersion populates the BPT diagram at a higher $[\text{NII}]/\text{H}\alpha$ ratio, in accordance with a shock scenario (Mingozzi et al. 2019, 2024).

4.2. J1010+1413

J1010+1413 ($z \sim 0.1992$) is one of the most luminous quasars at $z \sim 0.1$ – 0.2 in $[\text{OIII}]$ ($L_{[\text{OIII}]} \sim 1.69 \times 10^{43} \text{ erg s}^{-1}$). The HST/WFC3 *F621M* observation revealed a promising dual AGN candidate with the presence of two distinct $[\text{OIII}]$ emitting point sources with a projected separation of 430 pc

(Goulding et al. 2019). This cannot be probed with our MUSE observations (which have a resolution FWHM of ~ 2 kpc), as in the case of J1000+1242. The morphology and kinematics of J1010+1413 are really complex, as is shown also in the continuum image from HST/WFC3 *F689M* in Fig. 1. This is probably due to a recent merger (Goulding et al. 2019; Jarvis et al. 2021). $[\text{OIII}]$ shows strong emission around the nucleus and two lower-luminous $[\text{OIII}]$ (as well as in $\text{H}\alpha$, which we do not show) hotspots cospatial with the radio lobes (see Figs. 6 and 1). The source is also surrounded by a diffuse halo that is visible in the continuum (Fig. 1).

The velocity map of $[\text{OIII}]$ reveals two distinct gradients at different scales and with opposite signs. The first gradient is visible at scales of $\sim 2''$ around the nucleus in the NS direction, spanning a velocity range of 200 km s^{-1} and $\sim 0 \text{ km s}^{-1}$. The second gradient, at higher scales ($5''$), corresponds to the northern and southern radio lobes, which are characterized by blue- ($\sim -200 \text{ km s}^{-1}$) and redshifted ($\sim 200 \text{ km s}^{-1}$) velocity, respectively. The $[\text{OIII}]$ velocity dispersion map shows that the preferential direction of the high-velocity dispersion ($\sim 500 \text{ km s}^{-1}$) is aligned perpendicular to the two distinct gradients. This region extends for 20 kpc in the direction perpendicular to the radio jet, as in J1000+1242. Corresponding to the two lobes, the velocity dispersion is lower, as previously observed in other works (Shimizu et al. 2019; Venturi et al. 2021). The lower velocity dispersion suggests that the lobes could either trace collimated gas that is pushed by the radio jet or rotational gas of the disk that is ionized by the AGN. The decoupling of the narrow and broad components was not straightforward in the central region (within 2 – $3''$, i.e., 7 kpc from the nucleus) because all components that contribute to the line profile show a high velocity dispersion, with values over 300 km s^{-1} . However, we chose the value of 350 km s^{-1} as a reasonable threshold, which allowed us to separate the line profile into a blueshifted broader component (up to 500 km s^{-1}), which we identified as the outflow, and a redshifted narrower component ($< 350 \text{ km s}^{-1}$). Because the meaning of this narrower component in this central region is unclear and it has a sigma dispersion of up to 300 km s^{-1} at least, we also computed the energetics of the outflow by considering that all the emission is dominated by the outflow, and we also included the regions that correspond to the two radio lobes in the outflow component.

The maps of gas excitation show a bipolar region with higher $[\text{OIII}]/\text{H}\beta$ and lower $[\text{SII}]/\text{H}\alpha$ compared to the regions outside of the bicone (see Figs. 4 and 7). The regions northwest and southeast of the center have a lower ionization level with a higher value of $[\text{SII}]/\text{H}\alpha$ and lower value of $[\text{OIII}]/\text{H}\beta$. Moreover, regions with a lower velocity dispersion populate the BPT diagram at lower $[\text{NII}]/\text{H}\alpha$ ratio, as was also found in J1000+1242.

4.3. J1010+0612

J1010+0612 is the nearest quasar of our sample with $z \sim 0.098$ ($1'' \sim 2.3$ kpc). The $[\text{OIII}]$ line emission is detected in a region limited to the central 7–8 kpc from the nucleus, beyond which the $[\text{OIII}]$ flux becomes very faint. The $\text{H}\alpha$ flux is more extended and shows a companion galaxy located approximately 16 kpc away (Fig. 8, the left panels in first two rows). In contrast to CO observations with ALMA, no double peak is observed in the moment 0 map of $\text{H}\alpha$ and $[\text{OIII}]$ (Ramos Almeida et al. 2022). The kinematic map of $\text{H}\alpha$ (Fig. 8, central panel) reveals a blueshifted emission SE ($\sim 50 \text{ km s}^{-1}$) of the nucleus and a velocity close to $\sim 50 \text{ km s}^{-1}$ NW of the nucleus. This rotational pattern closely resembles that observed in the stellar velocity

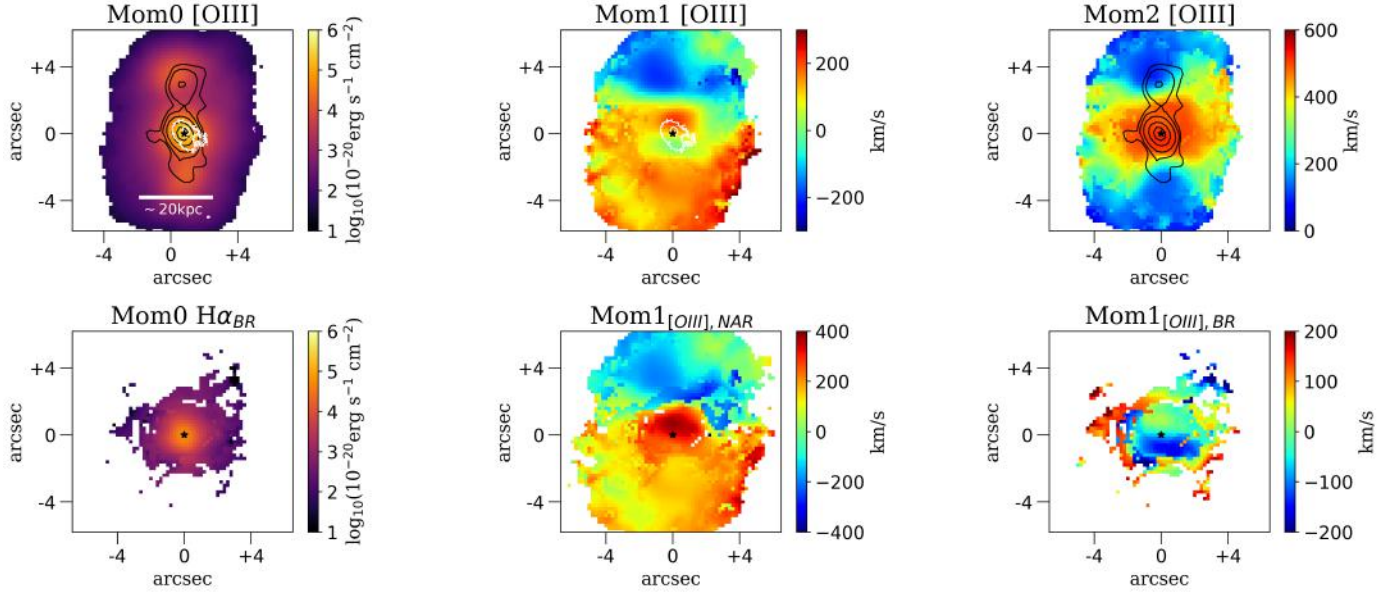


Fig. 6. Same as Fig. 3 for J1010+1413.

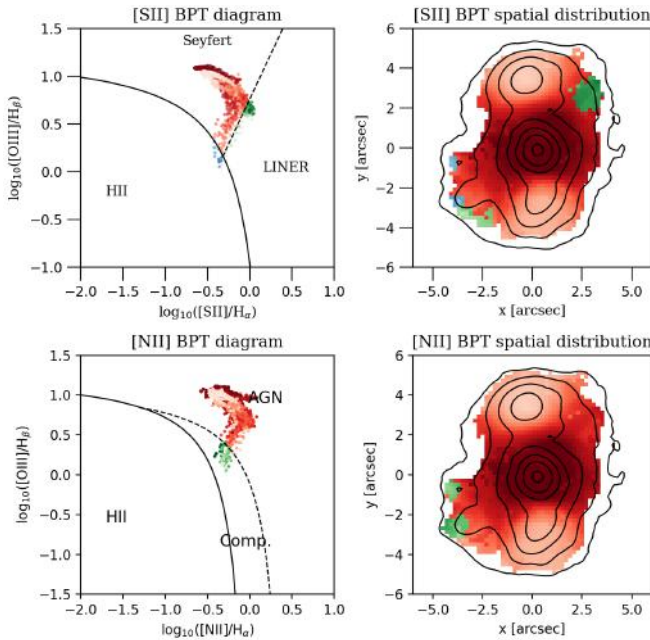


Fig. 7. Same as Fig. 5 for J1010+1413.

map (see Appendix A), but with lower absolute values. This discrepancy arises because the line profile, as shown in Fig. 2, is not just composed by the disk emission, but also includes a significant contribution from a blue wing, which contributes to blueshifting the global velocity in the region where the stellar component is receding. Unlike J1000+1242 and J1010+1413, it is not possible to clearly resolve a precise region with a higher-velocity dispersion, but the motion of the gas is highly disturbed overall throughout the central region (up to 10 kpc) of J1010+0612, showing a velocity dispersion of up to 500 km s^{-1} . In contrast, the moment 2 of the companion galaxy decreases, suggesting that the merging is still in an early stage. The two maps displayed in the bottom center and bottom right panels of Fig. 8 show the velocity maps of the narrow and broad components, respectively. The velocity map of the narrow emis-

sion ($V_{[\text{OIII}],\text{NAR}}$) shows a similar rotation as that detected in the stellar kinematics (see Appendix A), providing clear evidence that the narrow emission traces the ionized hydrogen from the disk. The same rotation pattern is also detected in CO(2-1) (Ramos Almeida et al. 2022). The velocity map of the broad emission instead exhibits a blueshifted emission ($V_{[\text{OIII}],\text{BR}} \sim 100 \text{ km s}^{-1}$) that we identify as the outflow. The resolved S-BPT and N-BPT show that the central region is completely ionized by the AGN, with $[\text{OIII}]/\text{H}\beta$ up to 8. The companion galaxy is primarily ionized by HII, as shown from S-BPT, and it falls into the composite region in the N-BPT (Fig. 9).

4.4. J1100+0846

J1100+0846 is a type 2 AGN that is hosted in a barred spiral galaxy. The high-resolution HST/WFC3 image (Fig. 1) reveals nuclear elongated emission ($\sim 0.4''$, i.e. $\sim 0.8 \text{ kpc}$) in a direction consistent with the radio structure identified by e-MERLIN. Different from the other galaxies, the $[\text{OIII}]$ and $\text{H}\alpha$ emissions show a different morphology (Fig. 10, top left and middle left panels). The $\text{H}\alpha$ traces the disk and spiral arms of the galaxy, while the $[\text{OIII}]$ emission shows a broad circularly symmetric emission around the nucleus that is only partially resolved. Clear differences in the two emissions are also observed in the moment 1 maps (Fig. 10, top center and middle center panels). The integrated $\text{H}\alpha$ velocity map mainly traces the rotation of the galaxy, while the $[\text{OIII}]$ velocity is low and close to the systemic velocity of the galaxy. The moment 2 maps reveal that in correspondence with the spiral arms, the $\text{H}\alpha$ velocity dispersion is low ($\sim 120 \text{ km s}^{-1}$), while in the central region, the gas shows high turbulence with velocity dispersions of up to 500 km s^{-1} in both $[\text{OIII}]$ and $\text{H}\alpha$ (Fig. 10, top right and middle right panels). However, it is unclear whether the high-velocity dispersion region lies perpendicular to the direction of the jet (determined by the nucleus and the bright hotspot located N/NW of the nucleus; see Fig. 1), as it is in J1000+1242 and in J1010+1413. We find that the $V_{\text{H}\alpha,\text{NAR}}$ map is considerably smoother than the $\text{H}\alpha$ integrated velocity, and it almost perfectly matches the rotating stellar velocity V_{STAR} (see Appendix A). The rotation pattern is consistent with ALMA observations of CO(2-1) in this case

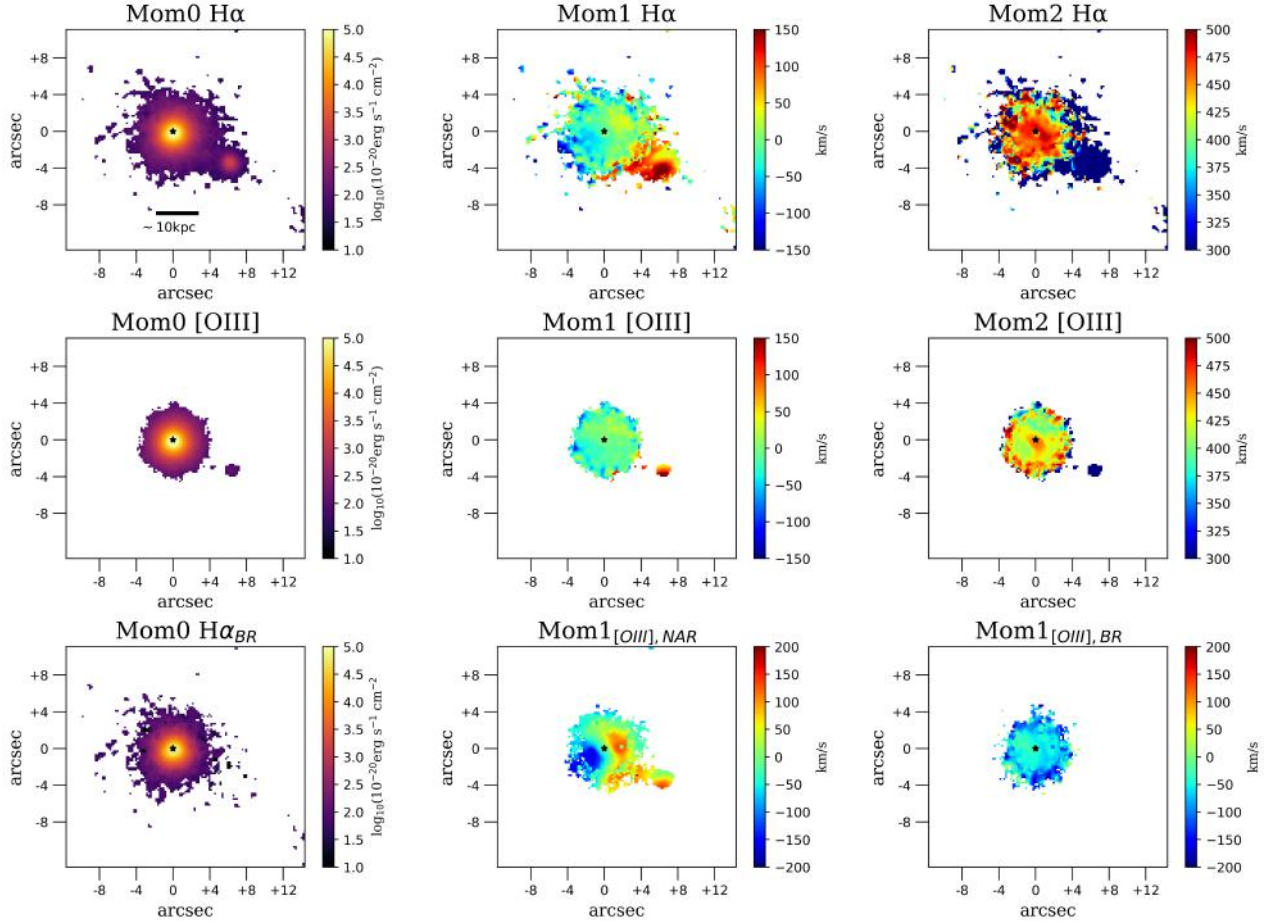


Fig. 8. Moment 0, 1, and 2 of Ha (top) and same as Fig. 3 for J1010+0612.

as well (Ramos Almeida et al. 2022). $V_{H\alpha, BR}$ resembles the first moment of [OIII]. This suggests that this high-velocity dispersion emission dominates the [OIII] line profile. We identify this emission as an outflow with a direction roughly in the plane of sky, given its low velocities in the line of sight (Fig. 10, middle center panel).

The S-BPT diagram reveals a constant value of [SII]/ $H\alpha$ in each spaxel, and the [OIII]/ $H\beta$ ratio spans a wide range of values, showing the highest values in the N-S direction, as also shown in Fig. 4. The ionization is dominated by AGN photons in most of the regions of the target. The same region populates the composite part of the N-BPT diagram (Fig. 11).

4.5. Extinction maps

To derive the extinctions, we measured the $H\beta/H\alpha$ line ratios from each spaxel and scaled them to calculate $E(B - V)$ as follows (Domínguez et al. 2013):

$$E(B - V) = \frac{2.5}{k(\lambda_{H\beta}) - k(\lambda_{H\alpha})} \log_{10} \left(\frac{(H\alpha/H\beta)_{\text{obs}}}{(H\alpha/H\beta)_{\text{in}}} \right), \quad (1)$$

where $k_{H\beta} \sim 3.7$ and $k_{H\alpha} \sim 2.5$ are the values of the extinction curve by Cardelli et al. (1989) at the $H\beta$ and $H\alpha$ wavelengths, respectively. We assumed $(H\alpha/H\beta)_{\text{in}} = 3.1$, typical of AGN (Veilleux et al. 1995). A_V is then calculated as $R_V \times E(B - V)$, where R_V (3.1) is the selective extinction, and it depends on the physical properties of the dust grains. We show the extinction maps without separating the kinematic components in Fig. 12.

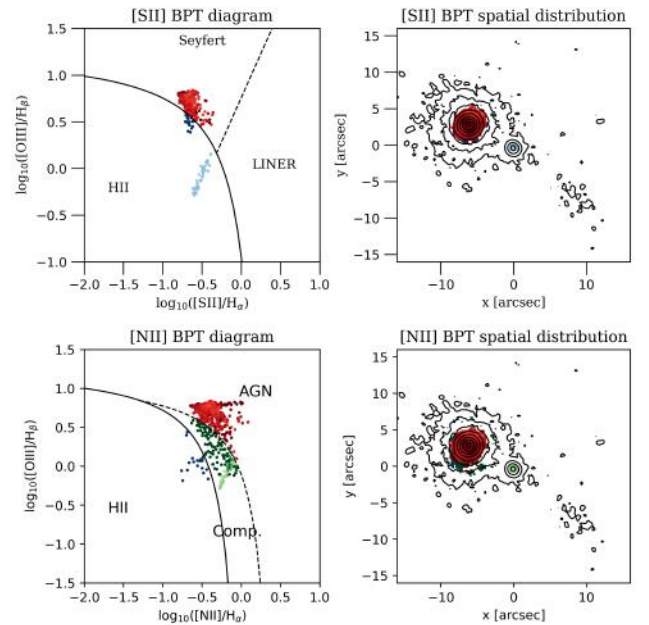


Fig. 9. Same as Fig. 5 for J1010+0612

The highest value of A_V in J1000+1242 is found in the nuclear region (~ 2.5 mag). For J1010+1413 and J1010+0612, we find almost constant values (~ 1.5 mag), except for a peak of the extinction in the southeast region of J1010+1413, which

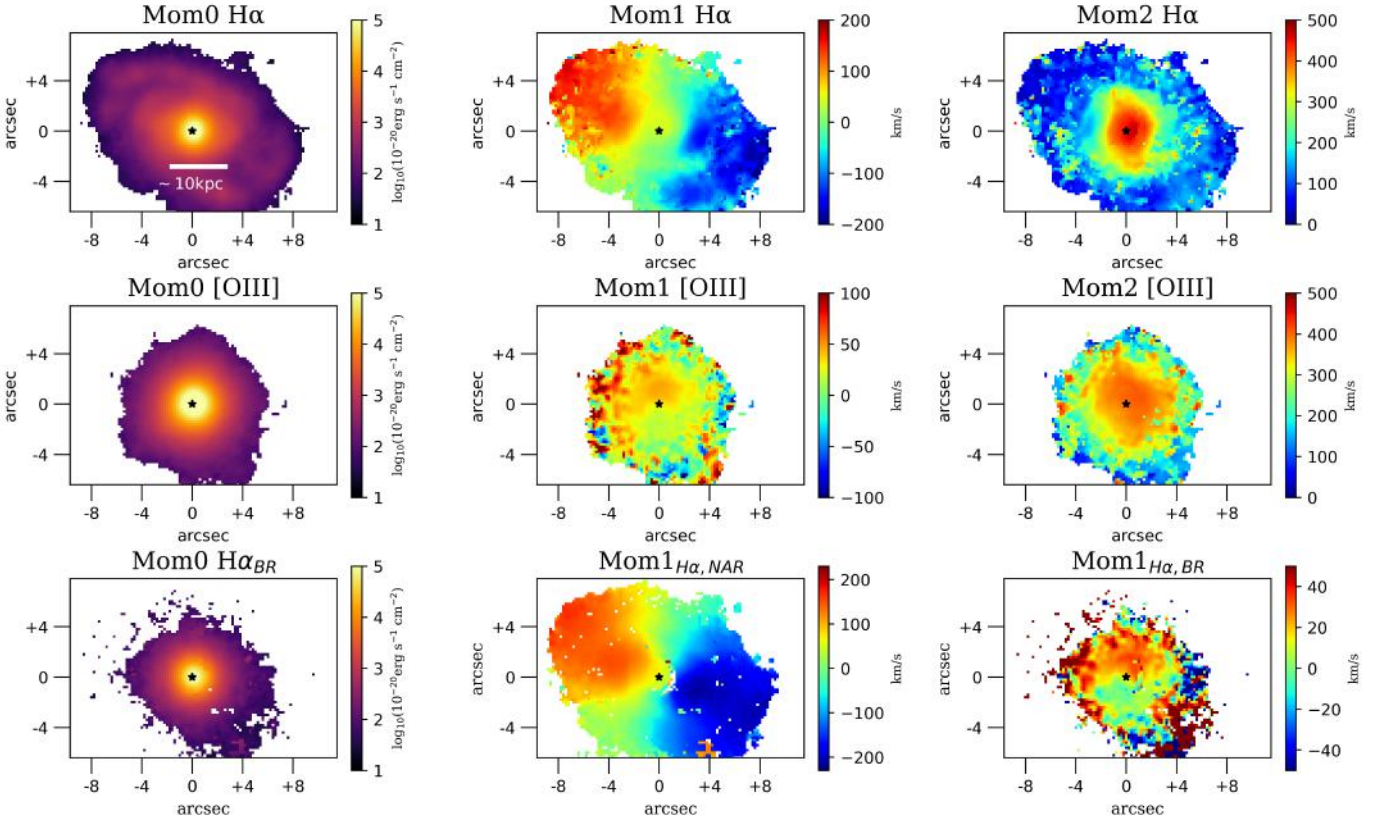


Fig. 10. Same as Fig. 8 for J1100+0846.

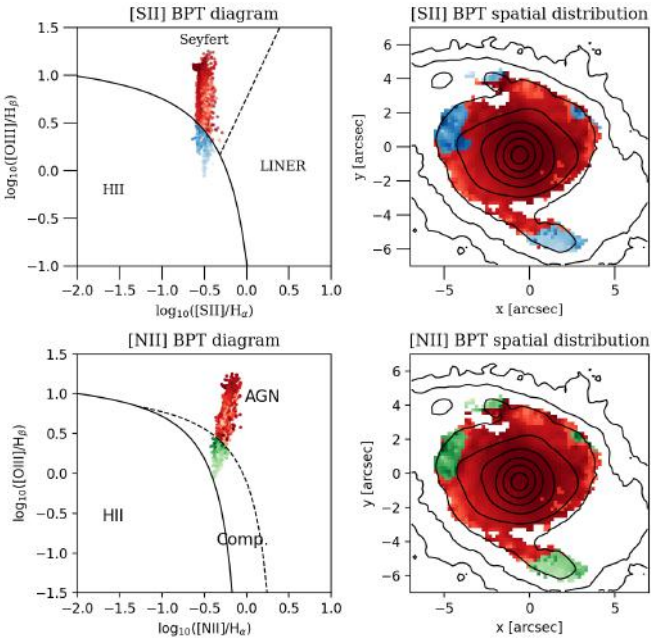


Fig. 11. Same as Fig. 5 for J1100+0846.

we previously identified as a region with lower ionization. For J1100+0846, we obtain a peculiar map of the extinction in which the higher values are found within $2''$ and $4''$ from the nucleus in the eastern region, corresponding to the higher molecular content of CO(2-1) found in Ramos Almeida et al. (2022). The mean extinction for all targets varies between 1 and 1.8 mag. We used these maps to correct for extinction the emission line fluxes in

our targets spaxel by spaxel. The corrected maps are not reported in this paper, but we used them to compute the properties of the ionized gas.

4.6. Properties of ionized outflows

The kinematic structures of the outflows in our objects are varied and complex. To characterize the physical properties of the outflows, we adopted the simplified model by Genzel et al. (2011), which is valid for case B recombination of fully ionized gas with $T \sim 10^4$ K.

The $H\alpha$ line luminosity can be expressed as

$$L_{H\alpha} = \int_V f n_e n_p j_{H\alpha}(n_e, T_e) dV, \quad (2)$$

where f is the filling factor, which is assumed to be 1, n_e is the electron density, $n_p = 1.2^{-1} \times n_e$ is the proton density assuming 10% number densities of He, and $j_{H\alpha}$ is the emissivity of $H\alpha$ at $T = 10^4$ K.

The mass of the outflowing gas is given by

$$M_{\text{out}}/M_{\odot} = 3.2 \times 10^5 \left(\frac{L_{H\alpha}}{10^{40} \text{ erg s}^{-1}} \right) \left(\frac{n_e}{100 \text{ cm}^{-3}} \right)^{-1}, \quad (3)$$

where we assumed no dependence between $j_{H\alpha}$ and n_e .

We determined the mass of the ionized outflows for each spaxel by considering in Eq. (3) only the contribution of the broad component of $H\alpha$. Then we summed all the contributions from all the spaxels to obtain the total mass of the outflow. The total outflow masses M_{out} derived for our sample range between $1 \times 10^7 M_{\odot}$ and $1 \times 10^8 M_{\odot}$. Assuming a simplified model of a conical outflow with an opening angle Ω , a radially constant

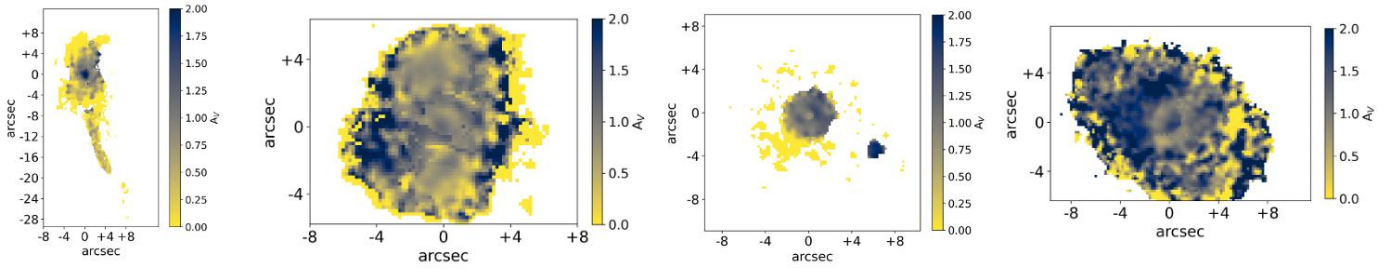


Fig. 12. Extinction maps from the Balmer decrement $H\alpha/H\beta$ (in units of magnitude). From left to right: J1000+1242, J1010+1413, J1010+0612, and J1100+0846. An S/N cut of 3 on the flux of each line has been applied to the maps.

Table 2. Properties of the high-velocity ionized outflow.

Name	$\log L_{\text{AGN}}^{(1)}$ [erg s^{-1}]	$M_{\text{out}}^{(2)}$ [$10^7 M_{\odot}$]	$n_{e,\text{out}}^{(3)}$ [cm^{-3}]	$R_{\text{out}}^{(4)}$ [kpc]	$v_{\text{out}}^{(5)}$ [km s^{-1}]	$\dot{M}_{\text{out}}^{(6)}$ [$M_{\odot} \text{yr}^{-1}$]	$\dot{E}_{\text{out}}^{(7)}$ [$10^{42} \text{erg s}^{-1}$]	$E_{\text{out}}^{(8)}$ [10^{56}erg]	$\epsilon^{(9)}$
J1000+1242	45.7	1.9	1230 ± 450	6	850 ± 115	2.9	0.7 ± 0.7	1.5 ± 0.5	4×10^{-4}
J1010+1413	46	5.2	360 ± 100	7	1190 ± 100	9.1	4 ± 2	7.4 ± 2.4	1.2×10^{-3}
		10		17		6.7	2.2	12.2	6.7×10^{-4}
J1010+0612	45.6	3.7	360 ± 100	7	1123 ± 155	6.2	2.6 ± 2.5	4.9 ± 1.5	2×10^{-3}
J1100+0846	46	5.3	336 ± 100	9	977 ± 120	6	1.8 ± 2.8	5.2 ± 2.5	5.5×10^{-4}

Notes. ⁽¹⁾AGN bolometric luminosity from [Harrison et al. \(2014\)](#). ⁽²⁾Total mass in outflow. ⁽³⁾Outflow electron density estimated from the [SII] doublet ratio. ⁽⁴⁾Outflow radius. ⁽⁵⁾Maximum outflow velocity, v_{max} , estimated as in [Fiore et al. \(2017\)](#). ⁽⁶⁾Mass outflow rate. ⁽⁷⁾Outflow kinetic power. ⁽⁸⁾Total energy in outflow. ⁽⁹⁾Coupling efficiency, $\dot{E}_{\text{out}}/L_{\text{AGN}}$. The second line for J1010+1413 reports the outflow properties obtained when considering that all the line emission comes from outflowing gas (see text in Sect. 4).

mass-loss rate, and an outflow velocity v_{out} , out to a radius R , we can compute the mass outflow rate as

$$\dot{M}_{\text{out}} = C \frac{M_{\text{out}} v_{\text{out}}}{R}, \quad (4)$$

where C depends on the adopted outflow history. In our case, we adopted a constant mass-outflow rate that led to $C = 1$ ([Lutz et al. 2020](#)). As an estimate of the radius of the outflow, we assumed the maximum extension of the blueshifted gas in the broad [OIII] component, defined as the distance at which the line flux reaches 10% of its total flux. We note that in all of our targets, this radius exceeds the seeing of the observations by more than three times. To estimate the electron density of the outflow, we employed the optical [SII] $\lambda 6717$ /[SII] $\lambda 6731$ ratio using the [Osterbrock & Ferland \(2006\)](#) theoretical relation, assuming a typical electron temperature of 10^4 K. We computed the density spaxel by spaxel using the broad component of [SII] resulting from the decoupling of the line profiles. To enhance the S/N, we integrated the flux of the [SII] doublet over the spaxels for which a physical density could be extracted, and we calculated an average density for the outflow. In the assumed scenario, the average volume density of the outflowing gas is proportional to R^{-2} , but in our case, we considered a mean value for the density. We used the PYNEB ([Luridiana et al. 2015](#)) software package to convert the doublet ratio into an electron density. The values of the outflow densities are reported in Table 2. To be consistent with other results in the literature ([Fiore et al. 2017](#); [Fluetsch et al. 2019](#)), we assumed that the bulk wind velocity is a combination of the velocity and the width of the outflow Gaussian component(s). In particular, we adopted the definition of the velocity in [Rupke & Veilleux \(2013\)](#) as

$$v_{\text{out}} = v_{\text{broad}} + 2\sigma_{\text{broad}}, \quad (5)$$

where v_{broad} is the central velocity of the broad component compared to the systemic velocity, and σ_{broad} is the velocity dis-

persion of the broad component. The concept is that when the line profile of the gas moves away, this appears as the combination of different velocities that are inclined at different angles with respect to our line of sight. Consequently, only the highest observed velocities represent the actual velocity of the outflowing material. We computed it in each spaxel in which the outflow was located, and we then calculated the average of the outflow velocities. We then assigned the standard deviation of the values in that region as the uncertainty on v_{out} .

We also computed the kinetic energy and the kinetic power of the outflow as $E_{\text{out}} = \frac{1}{2} M_{\text{out}} v_{\text{out}}^2$ and $\dot{E}_{\text{out}} = \frac{1}{2} \dot{M}_{\text{out}} v_{\text{out}}^2$, respectively. Their values are reported in Table 2 (see also [Speranza et al. 2024](#) for a comparison of outflow properties in J1010+0612 and J1100+0846). We also estimated the kinetic coupling efficiency, defined as $\epsilon = \dot{E}_{\text{out}}/L_{\text{bol,AGN}}$, finding values $\sim 10^{-3}$ – 10^{-4} , in accordance with values found in the literature ([Costa et al. 2018](#); [Harrison et al. 2018](#)).

5. Discussion

5.1. Comparison with ionized outflows in AGN in the literature

We compared our results with other works in the literature. [Fiore et al. \(2017\)](#) studied the dependence of the properties of outflows on the AGN bolometric luminosity in a sample covering $L_{\text{bol,AGN}}$ between $\sim 2 \times 10^{44} \text{erg s}^{-1}$ and $\sim 10^{48} \text{erg s}^{-1}$. For the targets presented in this work, we adopted the AGN bolometric luminosities calculated by [Harrison et al. \(2014\)](#) through mid- to far-infrared Spectral Energy Distribution (SED) fitting to archival photometric data.

The left and middle panels of Fig. 13 show the mass outflow rates and the kinetic powers as a function of $L_{\text{bol,AGN}}$. The black dots represent the sample of [Fiore et al. \(2017\)](#), who found a good correlation with L_{AGN} with log-linear slopes of 1.29 ± 0.38 and 1.50 ± 0.34 for the two above quantities,

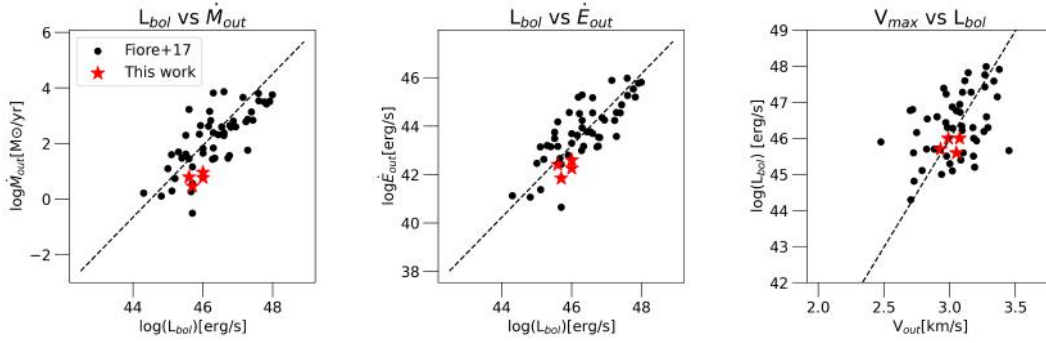


Fig. 13. Left: mass outflow rate as a function of the AGN bolometric luminosity. The black dots mark the ionized outflow measurements from [Fiore et al. \(2017\)](#), and red stars show our estimate for the four galaxies of our sample. The dashed black line is the best-fit correlation from [Fiore et al. \(2017\)](#) for their ionized outflow sample. Middle: kinetic power as a function of the AGN bolometric luminosity. Right: AGN bolometric luminosity as a function of the maximum outflow velocity.

respectively (dashed black lines). Although [Fiore et al. \(2017\)](#) used a lower value for the electron density (200 cm^{-3}) for all galaxies in their sample compared to the densities inferred in this work from [SII] (Table 2) and they assumed a decreasing mass outflow rate with time ($C = 3$), we found values for the mass outflow rates and the kinetic power (red stars in Fig. 13) that agree with those found for type 2 AGN with a similar bolometric luminosity ([Fiore et al. 2017](#)). In Fig. 13 we show the relation between AGN bolometric luminosity and the wind velocity, v_{out} , defined as in Eq. (5). The results for the AGN in our sample and those in Fig. 13 also agree well in this case.

5.2. Enhancement of the velocity dispersion perpendicular to the radio jet

By comparing the VLA radio maps at low resolution with the maps obtained from our analysis, we note a strongly enhanced gas velocity dispersion in the direction perpendicular to the jet in J1010+1413 and J1010+1242 (Fig. 14). The phenomenon is unclear in J1100+0846, and it is not observed in J1010+0612. In these cases, an enhanced velocity dispersion is detected in the central regions (Figs. 8 and 10), but the radio jet is poorly resolved or unresolved in the data, and thus, it is not straightforward to define a jet direction that can be compared with the high-velocity dispersion region.

We explore the possible origin for this phenomenon in the rest of this section.

5.2.1. Equatorial outflows

A possible explanation for the enhancement of the emission line width in the direction perpendicular to the radio jets could be an equatorial outflow (e.g., [Couto et al. 2014](#); [Riffel et al. 2015](#); [Freitas et al. 2018](#); [Shimizu et al. 2019](#); [Ruschel-Dutra et al. 2021](#)), which was predicted by some models to originate from the BH accretion disk. However, we observed significantly blue- and redshifted emission at each side of the nucleus, respectively, that we identified as high-velocity outflows, solely in the direction of the radio jet and the ionization cone. No net blue- or redshift of the broad component is detected instead in the elongated high-velocity dispersion region. Although no velocity shift is expected from a perfectly radial outflow without extinction, ionized outflows in QSOs commonly exhibit blueshifted wings, particularly in dusty objects, because the receding part of the outflow is located behind the host ([Bae & Woo 2014](#); [Carniani et al. 2015](#); [Balmaverde et al. 2016](#); [Woo et al. 2016](#),

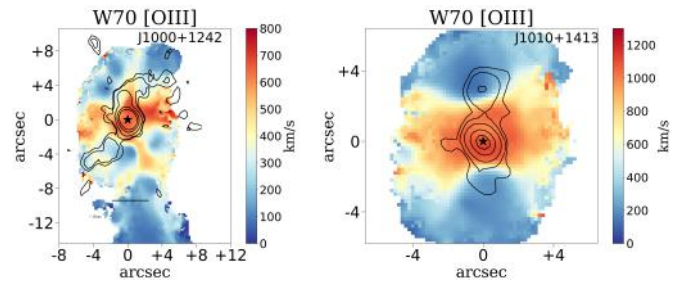


Fig. 14. Enhancement of [OIII] W70 perpendicular to the radio jet. The black contours represent the VLA low-resolution (~ 1 arcsec beam) radio emission at 6 GHz. J1100+0864 and J1010+0612 are not shown in this plot because the phenomenon studied is not evident due to the poorly resolved radio emission.

[2017](#); [Fiore et al. 2017](#)). Moreover, the fact that no clear velocity gradients (blueshifted on one side, redshifted on the other side) in these high-velocity dispersion regions have been observed in other works in the literature (e.g., [Venturi et al. 2021](#); [Ruschel-Dutra et al. 2021](#)), suggests that the enhancement of the velocity dispersion in the direction perpendicular to the jet and ionization cone is unlikely to be due to an equatorial outflow.

An alternative explanation is that the velocity dispersion enhancement could be the result of beam smearing, which could lead to the blending of spectral line profiles at different velocities along the line of sight, resulting in an increase in the velocity dispersion at the systemic velocity of the galaxy ([Durré & Mould 2019](#); [Shin et al. 2019](#)). We exclude the possibility of beam smearing because the scale on which we observe this line-width enhancement is larger than the spatial resolution of the observation.

5.2.2. Turbulence injected by the jet in the ISM

We conclude that the most plausible explanation for the observed phenomenon is interaction between the radio jet and the ISM of the host galaxy through the injection of turbulent energy in the direction perpendicular to the jet, consistent with [Venturi et al. \(2021\)](#). As discussed in that work, the increased velocity dispersion in an extended region perpendicular to the jet and ionization cone axis (along which high-velocity outflows are present) is only observed in galaxies hosting a radio jet, even when the radio power is low ($< 10^{44} \text{ erg s}^{-1}$).

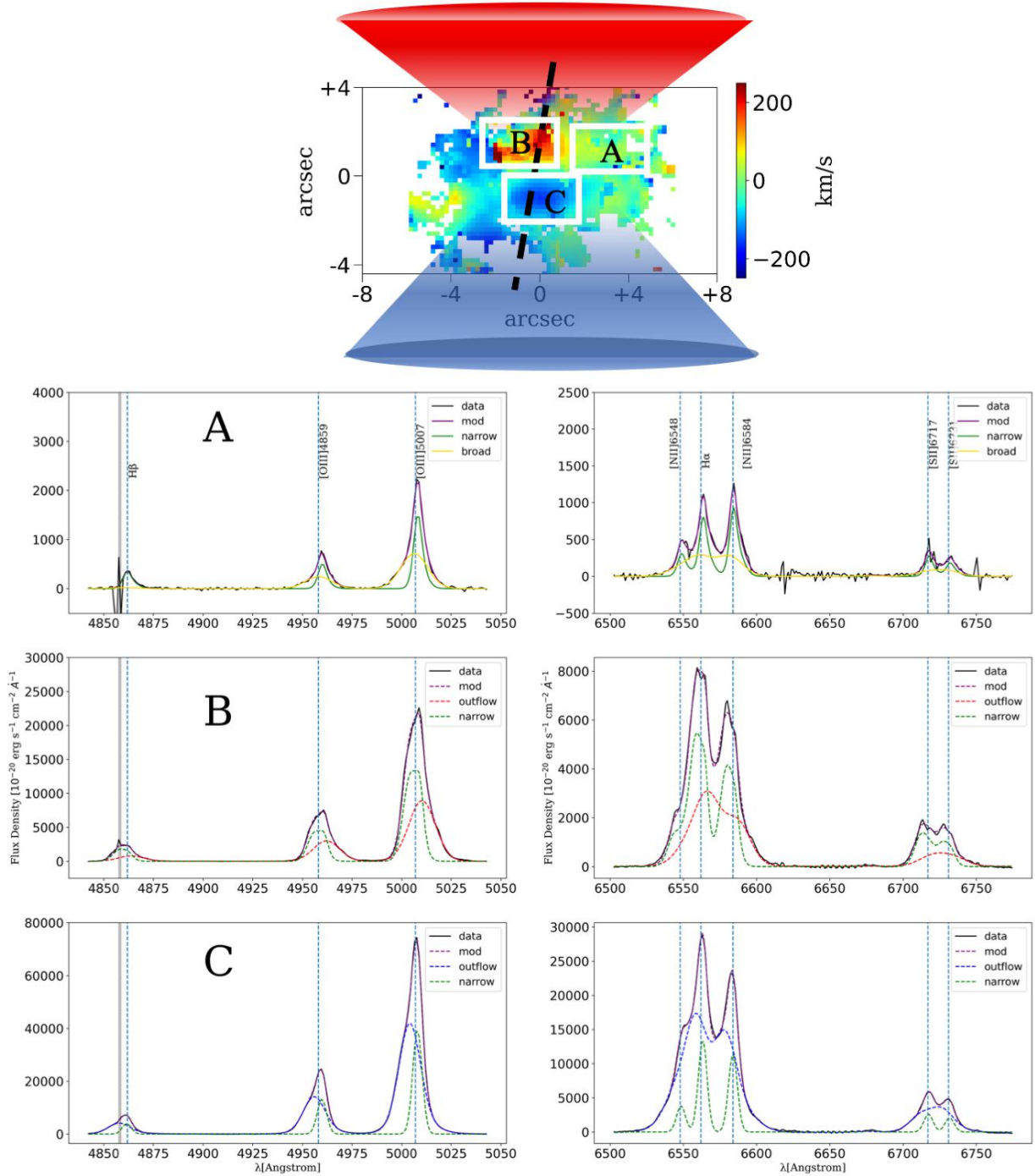


Fig. 15. Upper panel: Velocity of the broad component $V_{[\text{OIII}],\text{BR}}$ in J1000+1242, also reported in Fig. 3, zoomed in the central region. The axis of the outflowing bicone (traced by the red- and blueshifted motions in regions B and C, respectively) is parallel to that of the radio jet and ionization cones, while turbulent gas is located perpendicular to this (region A). The dashed black line indicates the direction of the radio jet. Bottom panels: integrated spectra extracted from the white rectangles in the corresponding subregions (A, B, and C) in the upper panel. Left panels: $\text{H}\beta$, $[\text{OIII}]$ doublet. Right panels: $\text{H}\alpha$ and the $[\text{NII}]$ and $[\text{SII}]$ doublets. The data are shown in black, the total best-fitting model is shown in purple, the narrow component is plotted in green, the broad component in region A tracing turbulent gas is shown in yellow, the redshifted outflow is shown in red, and the blueshifted outflow is shown in blue. The shaded gray area indicates the region that was excluded from the fit because the sky subtraction was too poor.

Figure 15 summarizes this scenario. The map at the top represents the velocity of the $[\text{OIII}]$ broad component (in J1000+1242) that we decoupled from the narrow component, as discussed in Sect. 3. We identify two regions with different properties. The first region lies parallel to the radio jet and to the ionization cones (labeled B and C), and the second region lies

perpendicular to the radio jet (labeled A). The former presents an $[\text{OIII}]$ velocity gradient of $\sim 400 \text{ km s}^{-1}$, tracing an outflow, while the latter exhibits an $[\text{OIII}]$ velocity close to the systemic velocity of the galaxy. Three representative spectra of the regions are shown in the figure. In the spectrum extracted from the southern outflowing cone (C), we observe a blue shifted wing (blue

Table 3. Properties of the radio jets and the ionized gas involved in the velocity dispersion enhancement perpendicular to the jets.

Name	$\log L_{1.4\text{GHz}}^{(1)}$ [W Hz ⁻¹]	$P_{\text{jet}}^{(2)}$ [10 ⁴³ erg s ⁻¹]	$P_{\text{jet}}^{(3)}$ [10 ⁴³ erg s ⁻¹]	$n_e^{(4)}$ [cm ⁻³]	$M_{\text{ion}}^{(5)}$ [10 ⁷ M _⊙]	$E_{\text{ion}}^{(6)}$ [10 ⁵⁶ erg]	$t_{\text{jet}}^{(7)}$ [Myr]	$E_{\text{jet}}^{(8)}$ [10 ⁵⁶ erg]
J1000+1242	24.2	8.3 ^{+2.5} ₋₂	7.3	510	7.5 ± 2.4	0.7 ± 0.3	7.5	195
J1010+1413	24	7.1 ^{+1.8} _{-1.5}	4.9	390	9.3 ± 2.5	2.1 ± 0.8	3.6	80
J1010+0612	24.4	9.8 ⁺³ _{-2.5}	10.9	280	6.1 ± 1.4	1.2 ± 0.5	0.04	1.2
J1100+0846	24.2	8.3 ^{+2.5} ₋₂	7.3	260	10 ± 2	1.4 ± 0.4	0.1	2.3

Notes. ⁽¹⁾Radio luminosity from [Jarvis et al. \(2019\)](#). ⁽²⁾Kinetic power of the jet estimated from its radio luminosity with Eq. (6) from [Bîrzan et al. \(2008\)](#). ⁽³⁾Kinetic power of the jet estimated from its radio luminosity with Eq. (7) from [Heckman & Best \(2014\)](#). ⁽⁴⁾Electron density from the [SII] doublet ratio. ⁽⁵⁾Mass of ionized gas computed with Eq. (3). ⁽⁶⁾Kinetic energy of ionized gas, $E_{\text{ion}} = M_{\text{ion}}\sigma_{\text{ion}}^2/2$. ⁽⁷⁾Jet traveling time. ⁽⁸⁾Total kinetic energy of jet $E_{\text{jet}} = P_{\text{jet}}t_{\text{jet}}$.

line) that represents the approaching outflow, and in the spectrum extracted from the northern outflowing cone (B), the broad component is redshifted. The spectrum extracted from the region perpendicular to the jet (A) instead presents a fairly symmetric profile with a high velocity dispersion that according to the interpretation discussed above is due to the turbulence injected by the jet in the ISM.

[Venturi et al. \(2021\)](#) reported that this phenomenon occurs exclusively in AGN hosting small-scale (~ 1 kpc) low-power ($\lesssim 10^{44}$ erg s⁻¹) radio jets with low inclinations ($\lesssim 45^\circ$) with respect to the galaxy disk ([Querejeta et al. 2016](#)). To our knowledge, no line-width enhancement perpendicular to the jet has been detected in galaxies whose radio jets are directed perpendicular to the galaxy disk. At most, an increased line width has been found on very small scales (~ 20 – 40 pc) around the jet base. At variance with [Venturi et al. \(2021\)](#), the angular resolution of our observations does not allow for the determination of the jet inclination with respect to the galaxy disk. Although the inclination of the jet cannot be quantified, the co-spatiality of radio hotspots with the most intense emission in ionized gas suggests that the jet and the ISM interact strongly. These aspects strongly suggest that the origin of the enhanced line width perpendicular to the radio jets could be the interaction between the jet and the ISM in the galaxy disk. In support of this scenario, the most recent hydrodynamic simulations of jet-ISM interaction show that when the inclination angle of the radio jet to the galactic disk is high, the radio jet can easily escape, without significant interaction with the disk and without widely broadening the line profile. When the jet is instead coplanar or at low inclinations angles to the disk, the jet remains trapped in the disk and strongly and extensively perturbs the ISM ([Mukherjee et al. 2016, 2018a,b; Meenakshi et al. 2022](#)). In the two targets that clearly exhibit turbulent motions perpendicular to the jet (J1100+0864 and J1010+0612), the morphology of the host galaxy is unclear due to the disturbances induced by the mergers. As a result, it is not straightforward to establish a correlation between this phenomenon and the inclination of the jet with respect to the galaxy disk in our sample.

Comparing the Seyfert galaxies presented by [Venturi et al. \(2021\)](#) and those analyzed in this work, we note that in the latter, the enhanced line velocity widths perpendicular to radio jets are detected over a much larger scale, ~ 10 kpc. The reason probably is that the power of the radio jets in the galaxies of our sample is higher by almost an order of magnitude than in the case of the Seyferts in their work, and for this reason, they are able to induce this phenomenon on a larger scale.

In order to test whether the described scenario is feasible from the energetic point of view, that is, whether the jets are

sufficiently powerful to drive the observed gas perturbations, we estimated the mass of the ionized gas M_{ion} that undergoes this phenomenon and compared it with the jet power. For a direct comparison with the results obtained by [Venturi et al. \(2021\)](#) at lower jet powers ($< 10^{44}$ erg s⁻¹), we computed the kinetic power of the jets through the following relation from [Bîrzan et al. \(2008\)](#):

$$\log P_{\text{jet}} = (0.35 \pm 0.7) \log P_{1400} + (1.85 \pm 0.10), \quad (6)$$

where P_{jet} is the jet kinetic power (in units of 10^{42} erg s⁻¹), and P_{1400} is its radio luminosity at 1400 MHz (in units of 10^{24} W Hz⁻¹), taken from [Jarvis et al. \(2019\)](#). In order to investigate a possible systematic effect in the estimation of P_{jet} , we used the relation in [Heckman & Best \(2014\)](#):

$$P_{\text{jet}} = 4 \times 10^{35} (f_W)^{3/2} (10 \times P_{1400})^{0.86} W, \quad (7)$$

where f_W is a factor that takes all the uncertainties into account and has a value ~ 20 ([Blundell & Rawlings 2000](#)). We find values of P_{jet} that are consistent with those found with Eq. (6), except for J1010-1413, which is slightly beyond the errors. The values are reported in Table 3.

To compute the mass, we first spatially integrated the H α flux from the MUSE maps from regions with [OIII] W70 > 300 km s⁻¹ (and $S/N > 3$) and calculated its luminosity. Then, we estimated the mass of the ionized gas through Eq. (3), considering all the emission of H α (not only the broad components) and computing the electron density from the ratio of the total emissions of the [SII] doublet lines, [SII] $\lambda 6717$ /[SII] $\lambda 6731$. By doing so, we included in the turbulent gas all the gas that contributes to the total line emission, which might also include spaxels containing emission from both outflows and disk. Although a clear spatial comparison of the enhanced velocity dispersions with the radio jets is not possible for J1010+0612 and J1100+0846, we computed the turbulent gas mass for these objects as well. They are reported in the plots with fainter markers.

Figure 16 reports the mass of turbulent gas versus the power of the jets. By plotting our sample together with the nearby Seyfert galaxies from [Venturi et al. \(2021\)](#), [Peralta de Arriba et al. \(2023\)](#), we see a correlation between the power of the jet and the turbulent gas mass. The correlation holding over more than one order of magnitude in jet power and ~ 3 dex in mass and kinetic energy suggests that more powerful jets are able to affect larger quantities of the ISM, and this supports the scenario in which jets cause the enhancement in the emission line width in the perpendicular direction. The best-fit relation is

$$\log(M_{\text{ion}}) = 2.4 \log(P_{\text{jet}}) - (98.5 \pm 0.25), \quad (8)$$

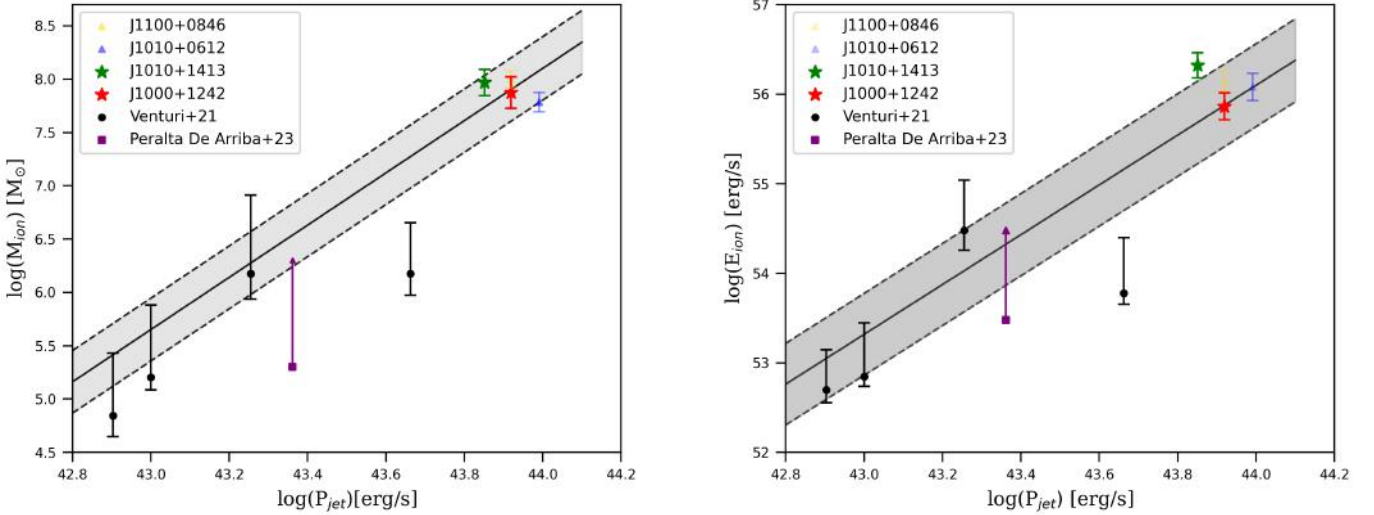


Fig. 16. Left: mass of the gas with a higher velocity dispersion ($[\text{OIII}] \text{ W70} > 300 \text{ km s}^{-1}$) as a function of the jet kinetic power. The black dots mark the ionized mass measurements from Venturi et al. (2021) for local Seyfert galaxies, while the colored symbols are our estimates for the ionized mass of the ionized gas in our sample. The stars are used for targets in which the higher velocity dispersion perpendicular to the jet is clearly observed, and the less transparent triangles are used for target in which this phenomenon is unclear, as for J1100+0864, or in which it is not observed, such as J1010+0612. The quantities have been calculated consistently with Venturi et al. (2021). The purple squares mark the measurements from Peralta de Arriba et al. (2023), which represent a lower limit of our estimations. Right: kinetic energy of the high-velocity dispersion gas as a function of jet kinetic power.

where M_{ion} is the mass of ionized gas in solar masses, and P_{jet} is the kinetic power of the jet in erg s^{-1} .

To be consistent with Venturi et al. (2021) and Peralta de Arriba et al. (2023), we estimated the kinetic energy of the gas in the same region as $E_{\text{ion}} = M_{\text{ion}} \sigma_{\text{ion}}^2 / 2$, where σ_{ion} is the velocity dispersion of $\text{H}\alpha$. We employed the velocity dispersion to calculate the ionized gas energy because it is an indicator of the turbulence produced by the radio jets. The right panel in Fig. 16 shows a correlation between the kinetic energy of the high-velocity dispersion gas and the kinetic power of the radio jets. This indicates that jets can inject energy into the ionized gas and can cause the enhancement of line emission. The best-fit relation is

$$\log(E_{\text{ion}}) = (2.62 \pm 0.01) \log(P_{\text{jet}}) - (59.7 \pm 0.4). \quad (9)$$

The correlations further support the scenario in which the jet injects turbulence in the ISM over a wide range of radio jet powers. In principle, this could be a significant mechanism of feedback because the high turbulence injected by the jet into the ISM could prevent the cooling of the gas and additional star formation (Mandal et al. 2021). The results are shown in Table 3.

To infer whether the jet is sufficiently powerful to be a viable mechanism of negative feedback, we compared the total kinetic energy produced by the jet E_{jet} in its traveling time t_{jet} with the energy computed for the high-velocity dispersion ionized gas E_{ion} . Assuming that the computed value of P_{jet} represents an average value over its traveling time, we can compute E_{jet} as $P_{\text{jet}} t_{\text{jet}}$ (Venturi et al. 2021). To estimate the jet traveling times, we used Eq. (A1) from Mukherjee et al. (2018b) with the same parameters as employed for IC5063, and we considered the jet radius as the largest linear size computed in Jarvis et al. (2021) (divided by 2). The traveling times and the kinetic energies of the jet are listed in Table 3. Dividing the total energy E_{ion} by the kinetic power of the radio jet E_{jet} , we find values of about 10^{-3} – 10^{-2} for J1000+1242 and J1010+1413. This indicates that the jet, with a low efficiency of energy transfer, is potentially capable

of injecting the required energy into the ISM and might cause the observed phenomenon in radio-quiet and luminous AGN as well. In J1010+0612 and J1100+0846, where the enhanced dispersion velocity is still high in the central region but is not observed in the direction perpendicular to the jet, the energies of the disturbed gas and the radio jets are comparable. For this reason, we cannot exclude for these targets either that the jet contributes to injecting turbulence into the ISM.

6. Conclusions

We presented a study of four luminous type 2 AGN (J1000+1242, J1010+1413, J1010+0612, and J1100+0846) with observations in the optical band obtained with the integral field spectrograph MUSE at VLT. These luminous AGN ($L_{\text{bol}} \sim 10^{46}$) are classified as radio quiet, although they host a moderate-power ($\sim 10^{44} \text{ erg s}^{-1}$) radio emission. To study the relation between the radio emission and the properties of the ionized gas, we combined our optical analysis with the radio analysis carried out by Jarvis et al. (2019) with VLA and e-MERLIN observations.

We investigated the kinematics of the ionized gas through the emission line profiles of $[\text{OIII}]5007$ and $\text{H}\alpha$. We identified the outflowing gas by decoupling a narrow emission component tracing the disk or tidal tails and a broad emission component tracing outflows and turbulent gas for all four targets. We detected extended outflows (up to 15 kpc) with high bulk velocities (up to 1000 km s^{-1}) that lie in the same direction as the jet and AGN ionization cones in the two targets with extended radio emission (J1000+1242 and J1010+1413). We computed the ionized outflow mass outflow rate and energetics by directly measuring the extinction and electron density in the outflow. We found $M_{\text{ion}} \sim 10^{7-8} M_{\odot}$, $\dot{E}_{\text{out}} \sim 10^{42-43} \text{ erg s}^{-1}$ and $\dot{M}_{\text{out}} \sim 10 M_{\odot} \text{ yr}^{-1}$.

The main result of our work is the detection of a strong (up to $\text{W70} \sim 1000 \text{ km s}^{-1}$) and extended (up to 20 kpc) emission line velocity width enhancement perpendicular to the direction of the

radio jets and of the AGN ionization cones in at least two targets of the sample. For the other two galaxies, the radio data are extended on smaller scales than we can probe with our MUSE data. The radio data therefore prevent a reliable assessment of the radio jet direction and interaction with the ISM. Other recent works (e.g., Venturi et al. 2021; Girdhar et al. 2022) observed the same phenomenon in other AGN hosting jets with a low kinetic power ($P_{\text{jet}} < 10^{44} \text{ erg s}^{-1}$). This was interpreted as due to the interaction between the jet and the ISM in the host galaxy disk.

Combining the results of our work and those of Venturi et al. (2021), we found a correlation between the kinetic power of the radio emission and the mass and energy of the ionized gas involved in the phenomenon, in accordance with the possible scenario of an interaction between the radio jet and the ISM. We found that the jets are powerful enough to inject the kinetic energy observed in the line width enhancement region into the ISM. This mechanism might represent an important channel of AGN feedback that needs to be taken into account. Moreover, the targets in which we detected this phenomenon have a higher bolometric luminosity and higher radio power emission than most objects in which this phenomenon was observed (but still lower than the powerful jets in radio-loud sources). This suggests that jets with low power might play a significant role in AGN feedback even in radiatively powerful sources (also see Girdhar et al. 2022). Through spatially resolved S-N BPT diagrams, we found that the main contribution to the ionization arises from the AGN photons, with an enhancement of [NII]/H α in the region with a high velocity dispersion perpendicular to the ionization cones. This may be ascribed to shocks due to the interaction between the jet and the ISM (Mingozzi et al. 2024).

However, to shed light on the effect of the radio jets on the host galaxy and further investigate the incidence and properties of the observed enhanced line widths perpendicular to the radio jets, a larger sample with high-quality integral field spectroscopic data is needed in the optical and IR bands to assess to which extent the phenomenon affects the molecular phase in addition to the ionized phase.

Acknowledgements. This article was produced while attending the PhD program in Space Science and Technology at the University of Trento, Cycle XXXVIII, with the support of a scholarship financed by the Ministerial Decree no. 352 of 9th April 2022, based on the NRRP – funded by the European Union – NextGenerationEU - Mission 4 “Education and Research”, Component 1 “Enhancement of the offer of educational services: from nurseries to universities” – Investment 4.1 “Extension of the number of research doctorates and innovative doctorates for public administration and cultural heritage”. GC, AM, GT, FM, FB, EB and GV acknowledge the support of the INAF Large Grant 2022 “The metal circle: a new sharp view of the baryon cycle up to Cosmic Dawn with the latest generation IFU facilities”. GC, AM acknowledge support from PRIN MIUR project “Black Hole winds and the Baryon Life Cycle of Galaxies: the stone guest at the galaxy evolution supper”, contract # 2017PH3WAT. EDT was supported by the European Research Council (ERC) under grant agreement no. 101040751. SC and GV acknowledge funding from the European Union (ERC, WINGS, 101040227). GV acknowledges support from ANID program FONDECYT Postdoctorado 3200802. CMH acknowledge funding from the United Kingdom Research and Innovation grant (code: MR/V022830/1).

References

Audibert, A., Ramos Almeida, C., García-Burillo, S., et al. 2023, *A&A*, **671**, L12
 Bae, H.-J., & Woo, J.-H. 2014, *ApJ*, **795**, 30
 Baldwin, J. A., Phillips, M. M., & Terlevich, R. 1981, *PASP*, **93**, 5
 Balmaverde, B., Marconi, A., Brusa, M., et al. 2016, *A&A*, **585**, A148
 Bianchin, M., Riffel, R. A., Storchi-Bergmann, T., Riffel, R., & Schonell, A. J. 2021, in *Galaxy Evolution and Feedback across Different Environments*, eds. T. Storchi Bergmann, W. Forman, R. Overzier, & R. Riffel, 359, 366

Birzan, L., McNamara, B. R., Nulsen, P. E. J., Carilli, C. L., & Wise, M. W. 2008, *ApJ*, **686**, 859
 Blundell, K. M., & Rawlings, S. 2000, *AJ*, **119**, 1111
 Cappellari, M., & Copin, Y. 2003, *MNRAS*, **342**, 345
 Cappellari, M., & Emsellem, E. 2004, *PASP*, **116**, 138
 Cardelli, J. A., Clayton, G. C., & Mathis, J. S. 1989, *ApJ*, **345**, 245
 Carniani, S., Marconi, A., Maiolino, R., et al. 2015, *A&A*, **580**, A102
 Cicone, C., Maiolino, R., Sturm, E., et al. 2014, *A&A*, **562**, A21
 Combes, F., García-Burillo, S., Casasola, V., et al. 2013, *A&A*, **558**, A124
 Costa, T., Rosdahl, J., Sijacki, D., & Haehnelt, M. G. 2018, *MNRAS*, **479**, 2079
 Couto, G. S., Storchi-Bergmann, T., Axon, D. J., et al. 2014, *Rev. Mex. A&A Conf. Ser.*, **44**, 191
 Cresci, G., Mainieri, V., Brusa, M., et al. 2015, *ApJ*, **799**, 82
 Cresci, G., Tozzi, G., Perna, M., et al. 2023, *A&A*, **672**, A128
 Dall’Agnol de Oliveira, B., Storchi-Bergmann, T., Kraemer, S. B., et al. 2021, *MNRAS*, **504**, 3890
 Domínguez, A., Siana, B., Henry, A. L., et al. 2013, *ApJ*, **763**, 145
 Durré, M., & Mould, J. 2019, *ApJ*, **870**, 37
 Fabian, A. C. 2012, *ARA&A*, **50**, 455
 Falcón-Barroso, J., Sánchez-Blázquez, P., Vazdekis, A., et al. 2011, *A&A*, **532**, A95
 Ferrarese, L., & Merritt, D. 2000, *ApJ*, **539**, L9
 Finlez, C., Nagar, N. M., Storchi-Bergmann, T., et al. 2018, *MNRAS*, **479**, 3892
 Fiore, F., Feruglio, C., Shankar, F., et al. 2017, *A&A*, **601**, A143
 Fluetsch, A., Maiolino, R., Carniani, S., et al. 2019, *MNRAS*, **483**, 4586
 Freitas, I. C., Riffel, R. A., Storchi-Bergmann, T., et al. 2018, *MNRAS*, **476**, 2760
 García-Burillo, S., Combes, F., Usero, A., et al. 2014, *A&A*, **567**, A125
 Gebhardt, K., Bender, R., Bower, G., et al. 2000, *ApJ*, **539**, L13
 Genzel, R., Newman, S., Jones, T., et al. 2011, *ApJ*, **733**, 101
 Girdhar, A., Harrison, C. M., Mainieri, V., et al. 2022, *MNRAS*, **512**, 1608
 Goulding, A. D., Pardo, K., Greene, J. E., et al. 2019, *ApJ*, **879**, L21
 Häring, N., & Rix, H.-W. 2004, *ApJ*, **604**, L89
 Harrison, C. M., Alexander, D. M., Mullaney, J. R., & Swinbank, A. M. 2014, *MNRAS*, **441**, 3306
 Harrison, C. M., Costa, T., Tadhunter, C. N., et al. 2018, *Nat. Astron.*, **2**, 198
 Heckman, T. M., & Best, P. N. 2014, *ARA&A*, **52**, 589
 Jarvis, M. E., Harrison, C. M., Thomson, A. P., et al. 2019, *MNRAS*, **485**, 2710
 Jarvis, M. E., Harrison, C. M., Mainieri, V., et al. 2021, *MNRAS*, **503**, 1780
 Kauffmann, G., Heckman, T. M., Tremonti, C., et al. 2003, *MNRAS*, **346**, 1055
 Kewley, L. J., Dopita, M. A., Sutherland, R. S., Heisler, C. A., & Trevena, J. 2001, *ApJ*, **556**, 121
 Kewley, L. J., Groves, B., Kauffmann, G., & Heckman, T. 2006, *MNRAS*, **372**, 961
 Kormendy, J., & Richstone, D. 1995, *ARA&A*, **33**, 581
 Kramida, A., Ralchenko, Yu., Reader, J., & NIST ASD Team 2023, *NIST Atomic Spectra Database (version 5.11)*, <https://physics.nist.gov/asd>
 Lamareille, F. 2010, *A&A*, **509**, A53
 Law, D. R., Ji, X., Belfiore, F., et al. 2021, *ApJ*, **915**, 35
 Luridiana, V., Morisset, C., & Shaw, R. A. 2015, *A&A*, **573**, A42
 Lutz, D., Sturm, E., Janssen, A., et al. 2020, *A&A*, **633**, A134
 Mandal, A., Mukherjee, D., Federrath, C., et al. 2021, *MNRAS*, **508**, 4738
 Marasco, A., Cresci, G., Nardini, E., et al. 2020, *A&A*, **644**, A15
 Marconi, A., Risaliti, G., Gilli, R., et al. 2004, *MNRAS*, **351**, 169
 May, D., & Steiner, J. E. 2017, *MNRAS*, **469**, 994
 May, D., Rodríguez-Ardila, A., Prieto, M. A., et al. 2018, *MNRAS*, **481**, L105
 May, D., Steiner, J. E., Menezes, R. B., Williams, D. R. A., & Wang, J. 2020, *MNRAS*, **496**, 1488
 McNamara, B. R., & Nulsen, P. E. J. 2012, *New J. Phys.*, **14**, 055023a
 Meenakshi, M., Mukherjee, D., Wagner, A. Y., et al. 2022, *MNRAS*, **516**, 766
 Mingozzi, M., Venturi, G., Mannucci, F., Marconi, A., & Cresci, G. 2019, *Commun. Byurakan Astrophys. Obs.*, **66**, 159
 Mingozzi, M., James, B. L., Berg, D., et al. 2024, *ApJ*, **962**, 28
 Molyneux, S. J., Harrison, C. M., & Jarvis, M. E. 2019, *A&A*, **631**, A132
 Mukherjee, D., Bicknell, G. V., Sutherland, R., & Wagner, A. 2016, *MNRAS*, **461**, 967
 Mukherjee, D., Bicknell, G. V., Wagner, A. Y., Sutherland, R. S., & Silk, J. 2018a, *MNRAS*, **479**, 5544
 Mukherjee, D., Wagner, A. Y., Bicknell, G. V., et al. 2018b, *MNRAS*, **476**, 80
 Mullaney, J. R., Alexander, D. M., Fine, S., et al. 2013, *MNRAS*, **433**, 622
 Nesvadba, N. P. H., Lehnert, M. D., De Breuck, C., Gilbert, A. M., & van Breugel, W. 2008, *ApJ*, **491**, 407
 Osterbrock, D. E., & Ferland, G. J. 2006, *Astrophysics of Gaseous Nebulae and Active Galactic Nuclei* (Sausalito, CA: University Science Books)
 Peralta de Arriba, L., Alonso-Herrero, A., García-Burillo, S., et al. 2023, *A&A*, **675**, A58
 Querejeta, M., Schinnerer, E., García-Burillo, S., et al. 2016, *A&A*, **593**, A118

- Ramos Almeida, C., Bischetti, M., García-Burillo, S., et al. 2022, *A&A*, **658**, [A155](#)
- Riffel, R. A., Storchi-Bergmann, T., & Riffel, R. 2014, *ApJ*, **780**, [L24](#)
- Riffel, R. A., Storchi-Bergmann, T., & Riffel, R. 2015, *MNRAS*, **451**, [3587](#)
- Rodrigo, C., Solano, E., & Bayo, A. 2012, *SVO Filter Profile Service Version 1.0*, [IVOA Working Draft 15 October 2012](#)
- Rodríguez-Ardila, A., Prieto, M. A., Mazzalay, X., et al. 2017, *MNRAS*, **470**, [2845](#)
- Rupke, D. S. N., & Veilleux, S. 2013, *ApJ*, **768**, [75](#)
- Ruschel-Dutra, D., Storchi-Bergmann, T., Schnorr-Müller, A., et al. 2021, *MNRAS*, **507**, [74](#)
- Sánchez-Blázquez, P., Peletier, R. F., Jiménez-Vicente, J., et al. 2006, *MNRAS*, **371**, [703](#)
- Shimizu, T. T., Davies, R. I., Lutz, D., et al. 2019, *MNRAS*, **490**, [5860](#)
- Shin, J., Woo, J.-H., Chung, A., et al. 2019, *ApJ*, **881**, [147](#)
- Silk, J., & Rees, M. J. 1998, *ApJ*, **331**, [L1](#)
- Speranza, G., Ramos Almeida, C., Acosta-Pulido, J. A., et al. 2024, *A&A*, **681**, [A63](#)
- Tozzi, G., Cresci, G., Marasco, A., et al. 2021, *A&A*, **648**, [A99](#)
- Vayner, A., Wright, S. A., Murray, N., et al. 2017, *ApJ*, **851**, [126](#)
- Veilleux, S., & Osterbrock, D. E. 1987, in NASA Conference Publication, ed. C. J. Lonsdale Persson, *NASA Conf. Pub.*, **2466**, [737](#)
- Veilleux, S., Kim, D. C., Sanders, D. B., Mazzarella, J. M., & Soifer, B. T. 1995, *ApJS*, **98**, [171](#)
- Venturi, G., Cresci, G., Marconi, A., et al. 2021, *A&A*, **648**, [A17](#)
- Venturi, G., Treister, E., Finlez, C., et al. 2023, *A&A*, **678**, [A127](#)
- Weilbacher, P. M., Palsa, R., Streicher, O., et al. 2020, *A&A*, **641**, [A28](#)
- Woo, J.-H., Bae, H.-J., Son, D., & Karouzos, M. 2016, *ApJ*, **817**, [108](#)
- Woo, J.-H., Son, D., & Bae, H.-J. 2017, *ApJ*, **839**, [120](#)
- Xu, C., Livio, M., & Baum, S. 1999, *AJ*, **118**, [1169](#)

Appendix A: Stellar kinematic maps

In Fig. A.1 we present stellar kinematic maps from the modeling with PPXF for J1010+0612 and J1100+0846 to compare them with the narrow component in Fig. 8 and 10. The σ was used to decouple the line profile between the narrow and broad

component (see text) in these two galaxies. In both galaxies, it is significantly higher in the central region (up to 5 kpc) and decreases in the outer regions (up to 20 kpc). In J1100+0846, the σ peaks west of the nucleus. The stellar maps are spatially smoothed using a Gaussian kernel with $\sigma = 1$ spaxel ($0.2''$) for clarity.

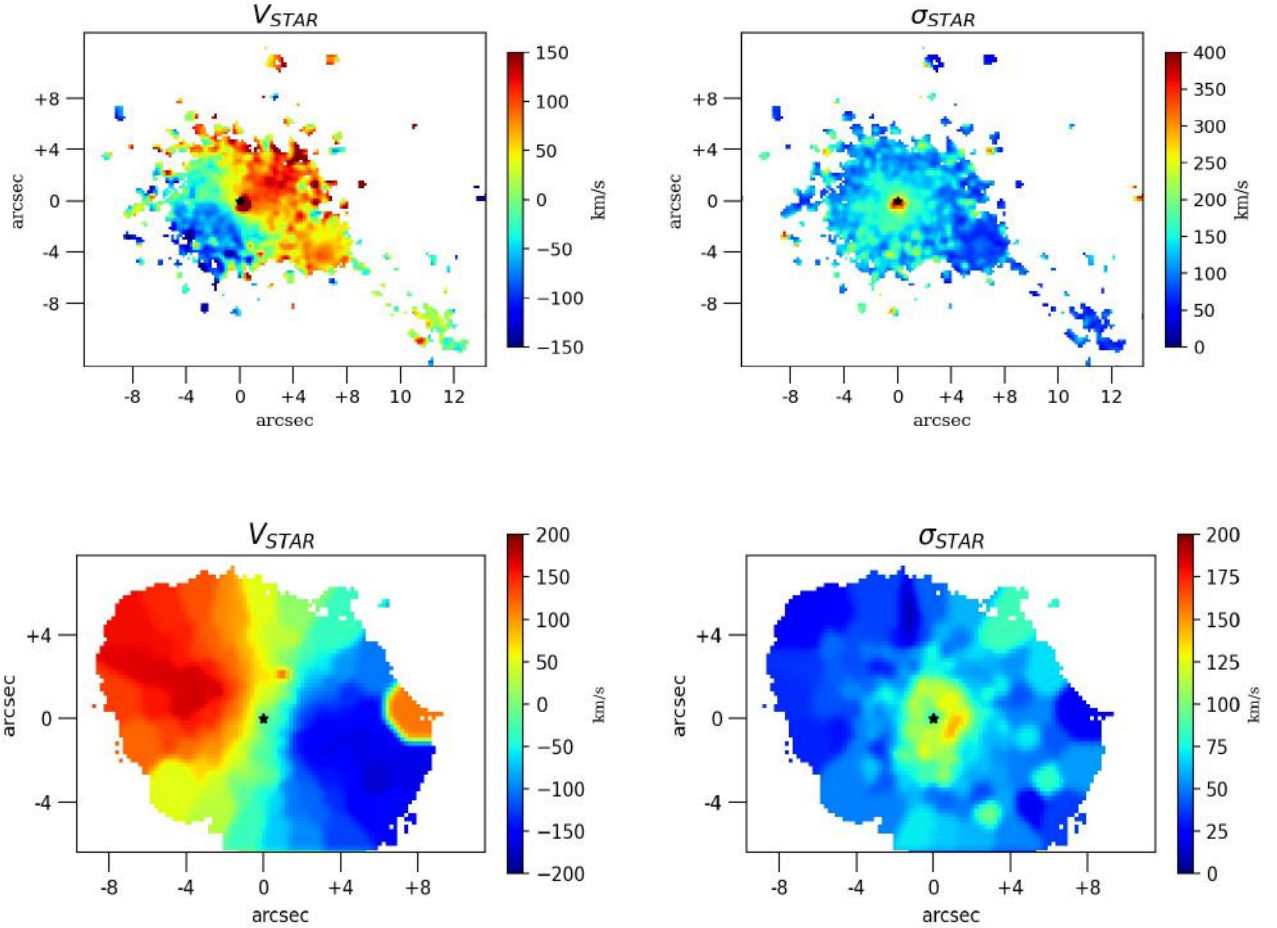


Fig. A.1. Stellar velocity and velocity dispersion computed with ppxf for J1010+0612 (top panels) and J1100+0846 (bottom panels).